NATIONAL TECHNICAL UNIVERSITY OF ATHENS

DIPLOMA THESIS

Multi-Harmonic Unbalance Response of Aircraft Jet Engine Rotors on Squeeze Film Dampers

Author:
Georgios Mitsos

Supervisor:
Athanasios Chasalevris

A thesis submitted in fulfillment of the requirements for the degree of Diploma in Mechanical Engineering

Athens, September 2022

Έχω διαβάσει και κατανοήσει τους κανόνες για τη λογοκλοπή και τον τρόπο σωστής αναφοράς των πηγών που περιέχονται στον οδηγό συγγραφής Διπλωματικών Εργασιών. Δηλώνω ότι, από όσα γνωρίζω, το περιεχόμενο της παρούσας Διπλωματικής Εργασίας είναι προϊόν δικής μου εργασίας και υπάρχουν αναφορές σε όλες τις πηγές που χρησιμοποίησα.

Οι απόψεις και τα συμπεράσματα που περιέχονται σε αυτή τη Διπλωματική εργασία είναι του συγγραφέα και δεν πρέπει να ερμηνευθεί ότι αντιπροσωπεύουν τις επίσημες θέσεις της Σχολής Μηχανολόγων Μηχανικών ή του Εθνικού Μετσόβιου Πολυτεχνείου.

Γεώργιος Μητσός

Foreword

Aircraft engine rotors are supported by rolling element bearings, usually ball and roller bearings. External damping is provided to rotors through Squeeze Film Dampers (SFDs). Moreover, test-rigs usually employ journal bearings for the driving motor. These three machine elements are in principle nonlinear with rotor displacement. However, linearization points can be identified, since they usually work in a linear area. Additionally, linearization helps for the parameter studies in the early design stages. Their linearization results in speed and bearing eccentricity dependent stiffness and damping values. In this work, the influence of speed and eccentricity dependent stiffness and damping on the rotor vibration is to be investigated. The main tasks are listed in the following:

- Introduction to the in-house rotor dynamic software of MTU & *MSC Nastran*
- Introduction to the rolling element bearing, squeeze film damper and journal bearing tool of MTU
- Literature review regarding linearization of nonlinear bearings
- Identification of necessary steps for linearization of all three machine elements
- Design and automatization of the complete linearization process
- Comparison of the results with literature
- Implementation of bearings with speed and/or eccentricity dependent stiffness and damping coefficients for a simple rotor in MTU's in-house tool for eigenfrequency and frequency response analyses
- Implementation of the above in *MSC Nastran* and comparison with MTU's in-house Tool
- Implementation of the above for a real engine
- Comparison of the results with those using constant coefficients
- Identification of eccentricity dependent bearing coefficients for usage in eigenfrequency analyses by using frequency response results and derivation of a pattern for normal unbalance cases
- Documentation of the results

The present master thesis started in National Technical University of Athens on October 2021 under the supervision of Assistant Professor Athanasios Chasalevris and, after five months, the thesis was continued in MTU Aero Engines AG in Munich, Germany for another six months under contract with the company, where was finalized on September 2022. During the time in MTU, the thesis was co-supervised by Dr. Ioannis Chatzisavvas.

Acknowledgements

I would really like to express my gratitude to Ioannis Chatzisavvas for mentoring me during my stay at MTU Aero Engines in Munich. I am grateful for his guidance, his immediate response every time I needed assistance and for the knowledge he offered me in the field of structural mechanics. I also want to thank him for helping me to adapt in a new environment, during my first days in Munich. My collaboration with him has been amazing!

Many thanks to Marcus Schrade for giving me the opportunity to work on such an interesting topic in an inspiring environment like MTU Aero Engines. I am also thankful to the rest of the team who have always been eager to help me with their knowledge.

The present thesis would not be possible without the huge support of my professor in Athens, Athanasios Chasalevris, who suggested that I apply for the position at MTU Aero Engines last year. His remarks and his advice were very important for the completion of the thesis.

And, of course, I cannot thank enough my friends and family back in Greece, who have always been there for me, as well as the new friends I made in Munich.

Abstract

The use of constant bearing stiffness and damping coefficients is common practice in the preliminary design stages of aircraft engines. Though linear analysis is especially time-efficient, it does not always provide accurate results. Hence, the effect of speed and eccentricity dependent bearing stiffness and damping on the dynamic behaviour of jet engines is examined in the present thesis. Jet engine rotors are usually supported by rolling element bearings, which may absorb axial thrust, but provide minimal damping. Therefore, squeeze film dampers are employed in order to provide additional external damping and avoid dangerous rotor vibrations. Rolling element bearings and squeeze film dampers typically introduce nonlinearities and speed dependent phenomena in the rotor system. Hence, their employ in the jet engine system is a crucial topic.

Methods concerning the linearization of journal bearings are very common in literature. Unfortunately, this is not the case with squeeze film dampers although they are widely used in aerospace industry for almost half a century. Therefore, a new multi-harmonic method is suggested for the solution of nonlinear systems in the frequency domain. The steps of the method are thoroughly explained in the present thesis. In brief, nonlinear bearing forces exerted on the casing and rotor(s) result from journal orbits. Afterwards, the forces along the orbit are approximated by harmonic functions utilizing Discrete Fourier Transform. Finally, the rotor response arises iteratively from the solution of as many systems of equations as the number of harmonics.

A Jeffcott rotor model and a realistic jet engine model are employed for the simulations conducted for the current thesis. The results of linear harmonic analysis with constant coefficients are compared to the transient response and they are proved to be extremely inaccurate. Therefore, the multi-harmonic method is applied for the calculation of the rotor unbalance response. In most cases presented, the results provided from the method are identical to the transient response, utilizing the first three or, even, just the first-order harmonic. A wide variety of cases are examined in order to verify the validity of the method. Specifically, cases of circular and elliptic orbits about either the centerline of the engine or off-centered points are presented. For the purposes of the thesis, a model based on the short bearing approximation is applied for the derivation of analytical formulas for the nonlinear forces exerted by squeeze film dampers. However, the multi-harmonic method is completely independent from the method applied for the calculation of the forces. Hence, any type or model of squeeze film damper and bearing can be used in combination with the method.

Finally, speed dependent bearings are employed in both models. The corresponding results of modal analysis and linear harmonic analysis are compared to the results of constant bearing coefficients. The application of speed dependent bearings proves to change significantly both the critical speeds and the amplitudes of the rotors.

Abstract (in Greek)

Η χρήση σταθερών στυντελεστών δυσκαμψίας και απόσβεσης εδράνων είναι συνήθης στα προκαταρκτικά στάδια σχεδιασμού αεροπορικών κινητήρων. Παρόλο που η γραμμική ανάλυση παράγει αποτελέσματα σε μικρό χρόνο, αυτά δεν είναι πάντα ακριβή. Ως εκ τούτου, η επίδραση της δυσκαμψίας και της απόσβεσης των εδράνων που μεταβάλλονται με την ταχύτητα περιστροφής και την εκκεντρότητα στη δυναμική συμπεριφορά αεροπορικών κινητήρων εξετάζεται στην παρούσα διπλωματική εργασία. Οι άξονες των κινητήρων συνήθως εδράζονται σε έδρανα κύλισης, τα οποία απορροφούν τα αξονικά φορτία της ώσης και τα δυναμικά ακτινικά φορτία λόγω αζυγοσταθμίας, αλλά παρέχουν ελάχιστη απόσβεση. Επομένως, χρησιμοποιούνται αποσβεστήρες συμπίεσης ελαίου στην ακτινική διεύθυνση ώστε να παρασχεθεί επιπλέον απόσβεση και να αποφευχθούν επικίνδυνες εγκάρσιες ταλαντώσεις των αξόνων. Τα έδρανα κύλισης και οι αποσβεστήρες συμπίεσης ελαίου εισάγουν στο περιστρεφόμενο σύστημα μη-γραμμικότητες και φαινόμενα που εξαρτώνται από την ταχύτητα περιστροφής. Ως εκ τούτου, η εισαγωγή τους σε έναν αεροπορικό κινητήρα είναι ένα κρίσιμο ζήτημα.

Μέθοδοι που αφορούν τη γραμμικοποίηση εδράνων ολίσθησης απαντώνται πολύ συχνά στη βιβλιογραφία. Αυτό δε συμβαίνει με τους αποσβεστήρες συμπίεσης ελαίου, παρόλο που χρησιμοποιούνται ευρέως στην αεροπορική βιομηχανία εδώ και σχεδόν μισό αιώνα. Για αυτό τον λόγο, μια νέα πολυαρμονική μέθοδος προτείνεται για τη λύση μη-γραμμικών συστημάτων στο πεδίο της συχνότητας. Τα βήματα της μεθόδου εξηγούνται λεπτομερώς στην παρούσα εργασία. Εν συντομία: υπολογίζονται οι μη-γραμμικές δυνάμεις των εδράνων σε διακριτά σημεία των τροχιών τους. Στη συνέχεια, οι δυνάμεις προσεγγίζονται από περιοδικές συναρτήσεις μέσω του Διακριτού Μετασχηματισμού Fourier. Τέλος, η απόκριση του άξονα προκύπτει επαναληπτικά από την επίλυση τόσων συστημάτων εξισώσεων όσο και ο αριθμός των αρμονικών.

Ένα μοντέλο άξονα Jeffcott κι ένα ρεαλιστικό μοντέλο αεροπορικού κινητήρα χρησιμοποιούνται για τις προσομοιώσεις της παρούσας εργασίας. Τα αποτελέσματα της γραμμικής αρμονικής ανάλυσης με σταθερούς συντελεστές συγκρίνονται με τη μεταβατική απόκριση και αποδεικνύονται εξαιρετικά ανακριβή. Επομένως, η πολυαρμονική μέθοδος εφαρμόζεται για τον υπολογισμό της απόκρισης αζυγοσταθμίας των αξόνων. Στις περισσότερες περιπτώσεις, τα αποτελέσματα της μεθόδου είναι πανομοιότυπα με αυτά της μεταβατικής απόκρισης, χρησιμοποιώντας μάλιστα τις πρώτες τρεις ή, ακόμα και, μόνο την πρώτη αρμονική. Εξετάζεται μια μεγάλη ποικιλία περιπτώσεων, συγκεκριμένα κυκλικές και ελλιπτικές τροχιές, γύρω από τη μέση γραμμή της μηχανής ή διαφορετικά, ώστε να πιστοποιηθεί η εγκυρότητα της μεθόδου. Για την παρούσα εργασία, ένα μοντέλο βασισμένο στην προσέγγιση στενών εδράνων εφαρμόζεται για τον υπολογισμό (αναλυτικό ή αριθμητικό) των μη-γραμμικών δυνάμεων. Παρόλαυτα, η πολυαρμονική μέθοδος είναι εντελώς ανεξάρτητη από τη μέθοδο που χρησιμοποιείται. Έτσι, οποιοσδήποτε τύπος ή μοντέλο εδράνου ή αποσβεστήρα συμπίεσης ελαίου μπορεί να χρησιμοποιηθεί σε συνδυασμό με τη μέθοδο.

Τέλος, εισάγονται στα δύο μοντέλα αξόνων έδρανα με συντελεστές που εξαρτώνται από την ταχύτητα περιστροφής. Τα αποτελέσματα της ιδιοδιανυσματικής και της γραμμικής αρμονικής ανάλυσης συγκρίνονται με αυτά των εδράνων με σταθερούς συντελεστές. Η χρήση αυτών των εδράνων μεταβάλλει σημαντικά την ποιότητα των αποκρίσεων των αξόνων.

Contents

List of Figures

List of Tables

List of Symbols

Vectors are symbolized by bold lowercase characters with underbars and matrices by bold uppercase characters.

Latin symbols

C	Damping matrix
c	Damping coefficient
c_r	Radial clearance
D	Diameter
e	Eccentricity
E	Young's modulus
F	Force
$\underline{\mathbf{f}}$	Force vector
G	Gyroscopic matrix
G	Balance quality grade
h	Oil film thickness
I	Identity matrix
j	Imaginary unit
K	Stiffness matrix
k	Stiffness coefficient
L	Length
M	Mass matrix
m	Mass
O	Center
P	Pressure
R	Radius
Re	Reynolds number

T	Period
t	Time
U	Unbalance
u, v, w	Velocity in x, y, z direction
X	Fourier transform
$\mathbf{0}$	Zero matrix
$\underline{\mathbf{0}}$	Zero vector

Greek symbols

Δ	Difference
ϵ	Eccentricity ratio
μ	Dynamic viscosity
$\underline{\mathbf{\Phi}}$	Eigenvector
ϕ	Angle
ρ	Density
θ	Angle
λ	Eigenvalue
Ω	Rotational speed
ω	Whirling speed

Subscripts and Superscripts

$(...)_b$	Bearing
$(...)_c$	Squirrel cage
$(...)_{cav}$	Cavitation
$(...)_{cr}$	Critical
$(...)_d$	Disk
$(...)_{des}$	Desired
$(...)_{dyn}$	Dynamic
$(...)_m$	Maximum value
$(...)_j$	Journal

$(...)_{per}$	Permissible
$(...)_{r}$	Radial direction
$(...)_{s}$	Shaft
$(...)_{sp}$	Specific
$(...)_{st}$	Static
$(...)_{str}$	Structural
$(...)_{t}$	Tangential direction
$(...)_{tot}$	Total
$(...)_{u}$	Unbalance
$(...)_{x}$, $(...)_{y}$, $(...)_{z}$	x, y, z direction
$(...)_{w}$	Weight
$(...)_{0}$	Initial condition
$(...)^{0}$	Initial estimation
$\dot{(...)}$	Derivative with respect to time

Abbreviations

DFT	Discrete Fourier Transform
DoF	Degree of Freedom
FEM	Finite Element Method
FW	Forward Whirling
HP	High Pressure
HPC	High Pressure Compressor
HPT	High Pressure Turbine
LP	Low Pressure
LPC	Low Pressure Compressor
LPT	Low Pressure Turbine
ODE	Ordinary Differential Equation
RHS	Right-Hand Side
RPM	Revolutions Per Minute
SFD	Squeeze Film Damper

1 Introduction

1.1 Aircraft Engine Overview

A jet engine is a reaction engine that provides thrust through jet propulsion. The compressor, the combustion chamber and the turbine are the main components of the gas generator. Gas generator provides high-pressure and high-temperature gas at its exit.

The thermodynamic process inside the engine follows Brayton cycle. As air passes through the rotating compressor, it is compressed. Afterwards, air and fuel are mixed and the mixture is burned in the combustion chamber. At this point, the fluid reaches its highest temperature. Subsequently, the turbine extracts energy from the fluid in order to rotate the compressor. Finally, the nozzle is used to convert the remaining internal energy of the mixture to kinetic energy.

In turbojet engines, all the air passes through the compressor, the combustion chamber, the turbine and the nozzle (core of the engine). On the other hand, turbofan engines have an additional large fan in the front. After the fan, air is split into two streams. The first one passes through the bypass nozzle and the other one through the core. The ratio of mass flow of the two streams is called bypass ratio [17, 26].

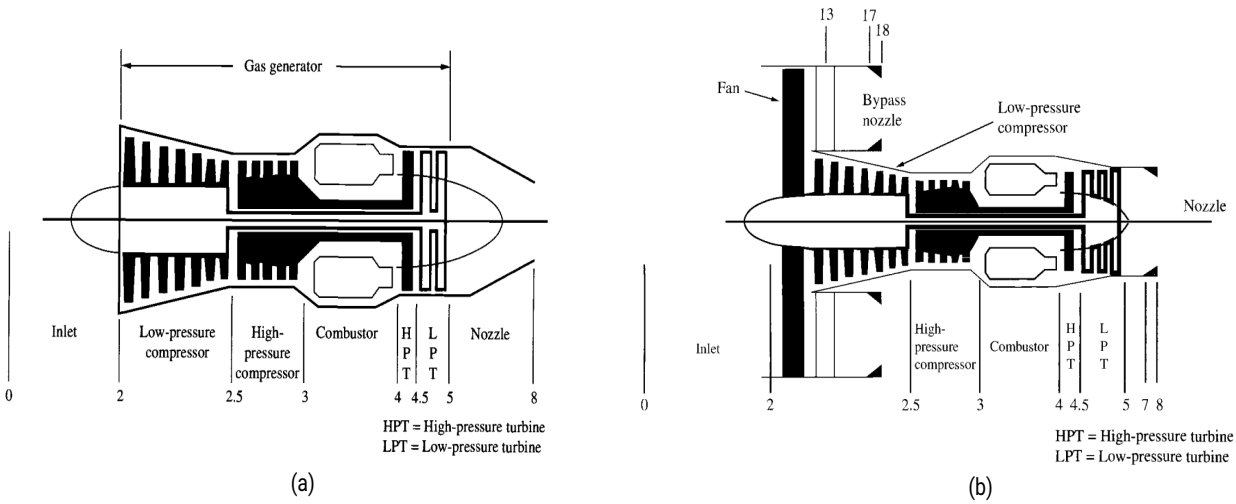

Figure 1.1: Diagram of a: a) dual-spool turbojet. b) high-bypass-ratio turbofan [26]

The most important components for the dynamic behaviour of aircraft engines are the rotor(s), the bearings and the casing. Jet engine rotors are rigid or flexible rotating shafts that consist of cylindrical and conical parts with several bladed disks mounted on them (fan, compressor and turbine stages). An engine, most commonly, has one (single-spool),

two (dual-spool) or, rarely, three (three-spool) shafts that may rotate either at the same or opposite direction. The casing is the stationary part of the engine and the bearings connect the rotors to the casing or to each other (inter-shaft bearings).

CFM56 is a dual-spool, high-bypass-ratio turbofan engine. The position of the bearings and compressor and turbine stages are presented in Fig. 1.2.

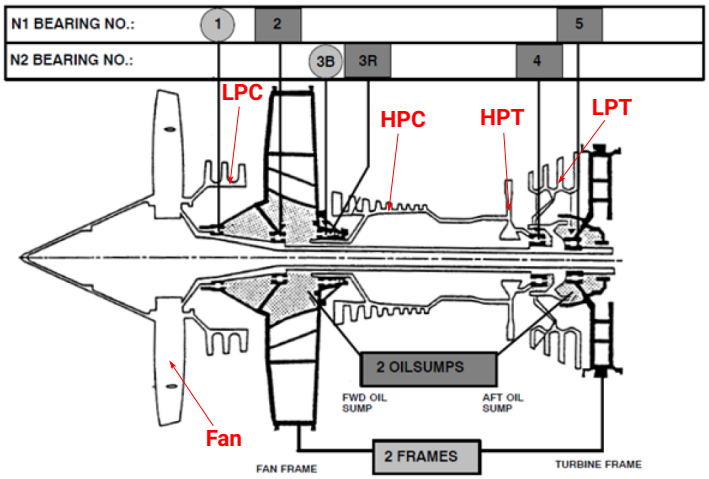

Figure 1.2: Bearings of the CFM56 engine [38]

1.2 Modeling of Jet Engines in Rotor Dynamics

Until some decades ago, the only way for the manufacturers to verify that their aircraft engines respected all necessary operational standards was the conduct of multiple expensive experiments. However, the development of computers and the increase of computational power currently allows them to perform highly accurate simulations, needed throughout the design process of aircraft engines.

Therefore, in order to be able to conduct all the necessary simulations and, ultimately, calculate the vibration of different engine parts, it is crucial to develop a model of the engine in an accurate and time-efficient manner. Generally, the model needs to sufficiently represent the properties of the real engine and, at the same time, not require an excessive amount of time to deduce results.

Finite Elements Method (FEM) combines these two characteristics and is considered to be the most reliable way to model engines for rotor dynamic simulations and solve the corresponding equations. The method is based on the division of continuous complex structures into smaller parts (finite elements). In such manner, the differential equations of the system are satisfied in a finite number of points (nodes). In order to ensure the compatibility of the whole structure, it is required that displacements are compatible to each other and the internal forces acting on multiple elements are in balance. The most important advantage of the FEM is the consideration of each element separately. In this way, its equations of motion are derived and, finally, all of them are assembled into a system of equations for the whole complex structure. Following the calculation

of displacements and forces for each node of the system, the same quantities are calculated for any other point of the structure via interpolation (most commonly polynomial interpolation) [28].

Although the Finite Element Method already existed for several years, Ruhl and Booker [36] and Nelson and McVaugh [30] were some of the first researchers to use it to model rotor systems. Nowadays, the literature about the application of FEM in rotor dynamics is vast.

There are many alternatives to the modeling of finite elements. One of the simplest and most popular approaches is the one-dimensional beam element modeling, but sometimes two or three-dimensional approaches are necessary in order to deduce more accurate results. For the purpose of rotor dynamic analyses, rotors and casing of jet engines are divided into a finite number of elements. When beam element methods are applied, each finite element has two nodes, one at each end, and each node is considered to have up to 6 degrees of freedom (DoFs), a displacement and a rotation about each axis (x, y, z). The most well-known one-dimensional FEM methods are Euler-Bernoulli beam theory and Timoshenko beam theory.

Rotor dynamic applications, especially those linked to high-speed rotating systems, such as aircraft engines, require a specific approach to the modeling process. General FEM codes do not take into account gyroscopic effects, which are crucial for rotor dynamic applications. Thus, some adjustments are necessary in order to be applied in rotor systems. Moreover, current trends in aerospace industry include lower weights and higher rotational speeds. These two characteristics tend to incommode the problems concerning the dynamic behaviour of the rotating machines [16].

The dynamic behaviour of rotating engines is seriously affected by some unique characteristics of them [15]. Because of incaccuracies during the assembly process of the engine, the presence of unbalance forces and moments is inevitable and leads to larger vibrations. Furthermore, stiffness and damping properties of bearings and squeeze film dampers (SFDs) are usually speed and eccentricity dependent. The gyroscopic phenomena are also influenced by the rotational speed and cause the natural frequencies of the engine to change with it.

In conclusion, aircraft engines are complex mechanical structures consisting of multiple machine elements and rotating in high speeds, which lead to complicated dynamic behaviour. They need to be designed to keep vibrations within limits that do not put the integrity of the engine into danger. In the event of intense rotor vibration, the radial clearance may prove to be insufficient. This may lead to contact between the rotating blades and the stationary part of the engine and, subsequently, destroy the blades. Also, high vibration is directly connected to extreme noise levels, through the transmission of the vibration to the supporting structures of the aircraft engine.

1.3 Bearing Models for Jet Engine Rotors

Bearings are used to support the rotors and connect them to the casing or to each other (inter-shaft bearings). Typically, aircraft engine rotors are supported by rolling element

bearings, mostly ball and roller bearings. Bearings operate in series with squeeze film dampers in aerospace applications, which are the main source of external damping applied on the rotor system. On the other hand, test-rigs usually employ journal bearings for the driving motor. All these types of bearings are designed for high rotating speeds and considerable supported loads.

The basic components of jet engines, as well as many design details of Trent 1000, are presented in Fig. 1.3. The position and the type of the bearings are also displayed. Trent 1000 is a three-soool, high-bypass-ratio turbofan engine that is produced by Rolls-Royce and powers Boeing 787 Dreamliner.

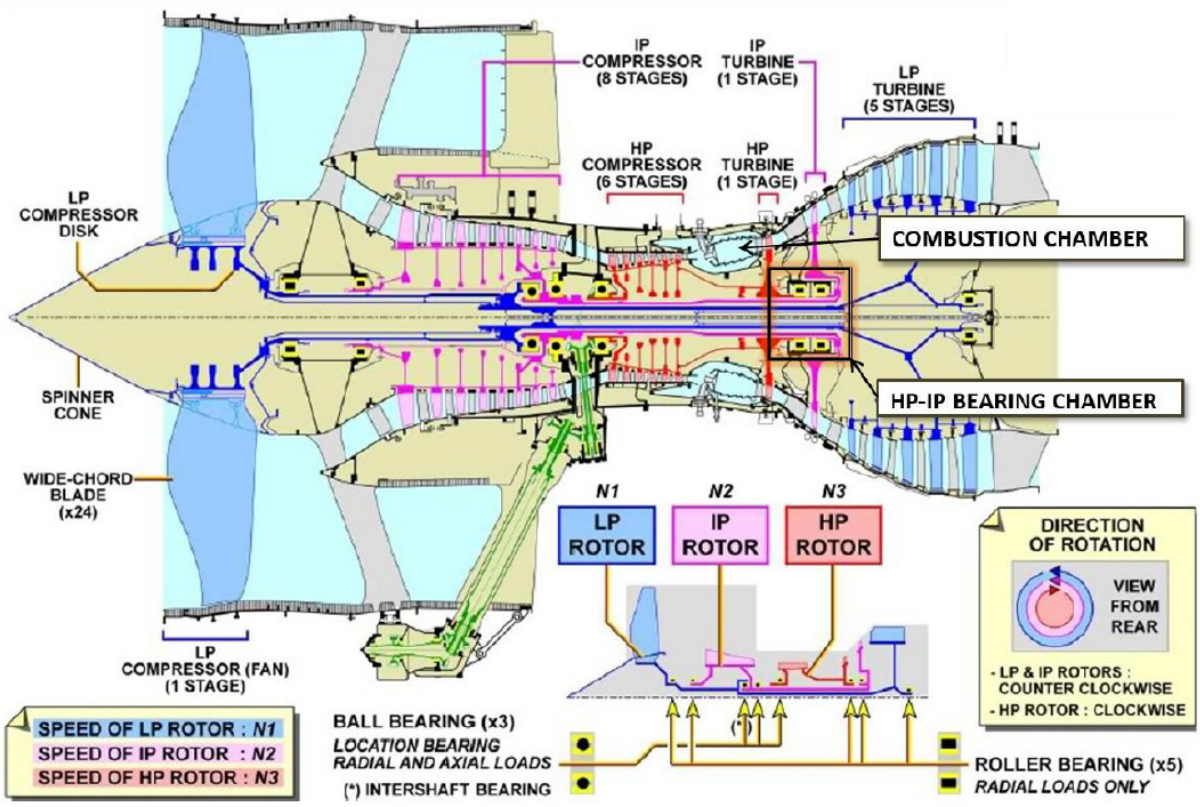

Figure 1.3: Bearings of the Rolls-Royce Trent 1000 engine [38]

Rolling element bearings are preferred in aerospace industry. Their main advantages are the long-lasting operation and the low power consumption because of their small friction. Moreover, they do not destabilize rotors, in contrast with journal bearings. However, they do not provide sufficient damping and it is usually necessary to operate with squeeze film dampers.

The presence of rolling element bearings in aircraft engines is mandatory. At least one of the bearings of every engine needs to be a thrust ball bearing in order to absorb all axial loads. Generally, rolling element bearings are modeled as linear speed-dependent springs in rotor dynamic applications. Roller bearings are 5-10 times stiffer than ball bearings [14].

Journal bearings are widely used in numerous large-scale engineering applications. Some characteristic examples are steam turbines, generators, compressors, internal combustion engines, and ship propulsion shafts. Journal bearings are capable of managing

shock more effectively than rolling element bearings. They are also quieter while running and tend to operate for larger periods of time as they are less prone to fatigue. Moreover, their operation is not easily disrupted by dirt and other particles. The advantages mentioned above originate from the journal bearing principle of operation: A thin oil film is use to support the journal. Finally, journal bearings require less radial space, yet more length in the axial direction [18].

Squeeze film dampers are mainly employed in aircraft engines in order to provide additional damping and prevent engine parts from undesired large vibration. Specifically, they operate in combination with rolling element bearings. They increase engine stability by isolating vibration, so it is not transited to other parts of the engine. In addition, they reduce rotor vibration and bearing wear. Their principle of operation is the same as journal bearings. Lubricant oil circulates around the radial gap between the journal and the housing. Due to journal motion, oil is constantly squeezed and displaced, which leads to the generation of oil film forces. In such manner, SFDs provide external damping and reduce rotor amplitudes of motion. However, the optimal amount of damping needs to be defined. Stiff SFDs rigidly connect the rotor and the casing and large forces are exerted on the latter. On the other hand, low damping may lead to uncontrollable journal motions and excessively large amplitudes.

Analytical overviews about the performance and the operation of squeeze film dampers have been published in the last decades. Della Pietra and Adiletta [2] present theoretical models and experimental results about various types of squeeze film dampers. In the second part of their article [3], they present recent improvements and innovative SFD designs. Moreover, in [8] common misconceptions about SFDs are pointed out and their dynamic behaviour is explained based on experimental data.

Zeidan et al. [41] present nonlinear phenomena that are regularly observed in SFDs, as well as practical issues about their implementation in aircraft engines. Furthermore, they analyze the most influential parameters for the performance of squeeze film dampers. The geometry (length, diameter and radial clearance) and oil characteristics (viscosity) are the most decisive factors for its operation. However, many other design parameters, such as seals type, cavitation profile along the oil film, supply pressure levels and fluid inertia, prove to be important, thus their effect has been studied in detail by many researchers.

Reinhardt and Lund [34] examine journal bearings and find out that the inclusion of the inertial term in the Reynolds equation leads to insignificant difference in the values of stiffness and damping coefficients, but introduce added mass coefficients that are important for small rotors.

Jung et al. [20], [21] investigate the influence of fluid inertia to both an open-ended and a partially sealed SFD through experimental procedures. The influence of oil inertia proves to be more important for the former, while the vapor cavitation affects both configurations, especially for small Reynolds numbers (small fluid inertia).

Concerning the influence of seals configuration, it is discovered that piston-ring seals provide larger damping forces than end seals and are less affected by the number of oil feeds [24]. Moreover, San Andrés [6] and San Andrés and Seshagiri [9] show that piston-ring sealed SFDs restrict the lubricant leakage and, as a result, produce remarkably larger damping and added mass coefficients than open-ended SFDs.

The configuration of a typical SFD, as well as the connection between the housing, the SFD, the rolling element bearing and the rotor, is presented in Fig. 1.4:

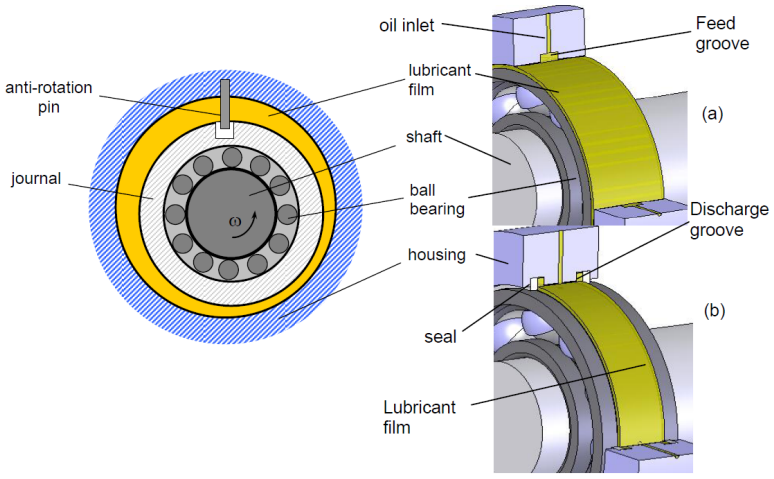

Figure 1.4: Squeeze film damper (SFD) configuration. a) SFD with central feed groove. b) SFD with end grooves and seals [5]

Bearings and SFDs are in principle speed dependent and nonlinear with rotor displacement. Hence, the general form of rotor-bearing system of equations is nonlinear and there is not a widely used systematic way for these systems to be solved in the frequency domain, even numerically.

This means that linear analysis is not feasible, unless bearings and SFDs are introduced in the dynamic models as linear elements. In this case, linearized stiffness, damping and mass coefficients (constant or speed dependent) are used as approximation and the engine unbalance response is calculated with low computational cost, but sometimes with debatable accuracy. All in all, there is an important trade-off between accuracy and time-efficiency concerning linearization. Linearization methods can only be applied to bearing coefficients under some strict conditions: They are valid for small perturbations about a fixed point, thus their extension to cases of large amplitude motions is likely to produce completely inaccurate results.

The linearization methods for squeeze film dampers are based on those for journal bearings. Lund [25] presents a linearization method applied on journal bearings and concludes that the results of unbalance response are satisfying for amplitudes as large as 40% of the radial clearance. Sawicki and Rao [37] also examine the limits of linearized stiffness and damping bearing coefficients. Krodkiewski [22] explains in detail the linearization process of multi-bearing rotor systems and compares the results to those of the nonlinear model. On the other hand, Nataraj and Nelson [29] propose another approach to the problem of nonlinear systems of multiple DoFs by solving linear and nonlinear equations separately in significantly less computational time.

Although the linearization process of journal bearings is clearly well documented, this is not the case for SFDs. Although squeeze film dampers are used in aircraft applications for more than 40 years, their linearization was only examined recently in [7], where dynamic stiffness coefficients are calculated by the journal orbit.

Linearized models may provide accurate enough or, even, excellent results but nonlinearities often become so important for the dynamic behaviour of the system that linear models are not sufficient. Nonlinear effects may originate from cracked rotors, rolling element bearings, squeeze film dampers, large deflections of the rotor and contacts with the stator. The results of the nonlinearities are jump phenomena, subharmonic resonances, chaotic vibrations and limit cycles [19].

In some cases, it is not feasible to assume a steady-state solution in order to solve a linear (or linearized) system, hence the problem needs to be solved in the time domain and then transient analysis is almost always preferred. Nevertheless, transient analysis is extremely time-consuming, especially for real aircraft engines, systems with hundreds or, even, thousands degrees of freedom. Consequently, it is not the ideal solution and cannot be used in the preliminary design stages of aircraft engines, where design parameters continuously change and fast, yet accurate, results are required.

Hence, a new multi-harmonic method to solve nonlinear systems in the frequency domain is introduced in the present thesis. The method is basically a variation of the classic linear harmonic analysis for higher-order harmonics too.

Linearized SFD forces are calculated based on journal orbits, through an iterative process. The main difference of the new method is the introduction of higher-order harmonic terms in order to sufficiently approximate nonlinear forces. The current thesis deals with SFD forces but its approach is general and can be used on any SFD type or model, e.g. including or excluding seals. Moreover, the method can be extended to other types of nonlinear bearings following all the advantages and limitations of the harmonic balance method. All in all, the method combines the advantages of linear harmonic analysis and transient analysis, since it is significantly faster than the latter and equally accurate, at the same time.

The content of the Chapters is briefly explained:

In **Chapter 2**, the theoretical background for the following contents of the thesis is provided. Common types of rotor dynamic analysis are briefly explained. Subsequently, analytical expressions for SFD impedance forces are derived from Navier-Stokes equations and are approximated using Discrete Fourier Transform (DFT). The solution of both mono-harmonic and multi-harmonic linear systems is provided. Finally, unbalance excitation for rotor systems is defined.

In **Chapter 3**, the equations of motion for a linear Jeffcott rotor model are derived and linear analysis is conducted for both constant and speed dependent bearings. Furthermore, the algorithm of the multi-harmonic method is explained in detail and is applied to the Jeffcott rotor model. Corresponding results are presented for a wide variety of cases and are compared to transient response in order to validate the method.

In **Chapter 4**, a realistic aircraft engine model is examined. Linear results (modal parameters and unbalance response) are presented. Afterwards, linear and nonlinear results are compared to each other for cases of centered orbits. Finally, results of the multi-harmonic method are presented for cases of off-centered orbits.

In **Chapter 5**, the principle ideas of the thesis are summarized and conclusions about the accuracy and the efficiency of the multi-harmonic method, as well as further improvements, are discussed.

2 Theoretical Background in Rotor Dynamics

2.1 Analytical Models for Shafts Vibrations

There is a broad variety of different types of analysis in the field of rotor dynamics. As mentioned in the introduction, a system may be described from either linear or nonlinear Ordinary Differential Equations (ODEs). Also, it may be stimulated from static, periodic or, generally, dynamic external forces. Therefore, the most suitable type of analysis may vary [40]. [15], [16], [23] thoroughly present the field of rotor dynamics.

2.1.1 Modal Parameters and Critical Speeds

Eigenanalysis calculates the eigenvalues and the eigenvectors of a linear dynamic system. Eigenfrequencies or natural frequencies are those frequencies at which the system is prone to vibrate in the absence of externally applied forces. When vibrating at a certain eigenfrequency, the system deforms into a corresponding shape (mode), which is described by the eigenvector. Eigenfrequencies are calculated as the imaginary part of complex eigenvalues.

A typical jet engine can be represented by the simplified model of Fig. 2.1.

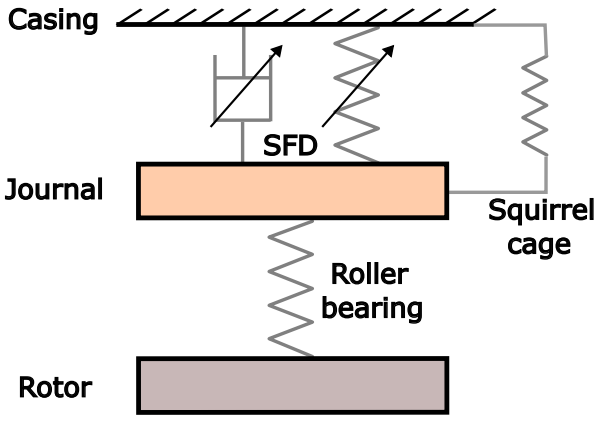

Figure 2.1: Simplified model of jet engine

The squeeze film damper operates in parallel with the squirrel cage and in series with the rolling element bearing.

The application of FEM on aircraft engines leads to the typical form of ODE system in rotor dynamics:

$$\mathbf{M} \cdot \underline{\ddot{\mathbf{x}}} + (\Omega\mathbf{G} + \mathbf{C}) \cdot \underline{\dot{\mathbf{x}}} + \mathbf{K} \cdot \underline{\mathbf{x}} = \underline{\mathbf{f}} \,, \tag{2.1}$$

where **M**, **G**, **C**, **K** are the symbols for mass, gyroscopic, damping and stiffness matrices. $\underline{\mathbf{x}}$ is the vector that represents the degrees of freedom (displacements and rotations) of the system and $\underline{\mathbf{f}}$ is the vector of external forces.

However, a system with no external forces is examined in eigenanalysis. The appropriate system to consider is the following:

$$\mathbf{M} \cdot \underline{\ddot{\mathbf{x}}} + (\Omega\mathbf{G} + \mathbf{C}) \cdot \underline{\dot{\mathbf{x}}} + \mathbf{K} \cdot \underline{\mathbf{x}} = \underline{\mathbf{0}} \tag{2.2}$$

The Eq. 2.2 is tranformed to a first-order system of differential equations [27]:

$$\mathbf{A} \cdot \frac{d}{dt} \begin{bmatrix} \underline{\mathbf{x}} \\ \underline{\dot{\mathbf{x}}} \end{bmatrix} + \mathbf{B} \cdot \begin{bmatrix} \underline{\mathbf{x}} \\ \underline{\dot{\mathbf{x}}} \end{bmatrix} = \begin{bmatrix} \underline{\mathbf{0}} \\ \underline{\mathbf{0}} \end{bmatrix} \,, \tag{2.3}$$

where:

$$\mathbf{A} = \begin{bmatrix} (\Omega\mathbf{G} + \mathbf{C}) & \mathbf{M} \\ \mathbf{M} & \mathbf{0} \end{bmatrix} \quad , \quad \mathbf{B} = \begin{bmatrix} \mathbf{K} & \mathbf{0} \\ \mathbf{0} & -\mathbf{M} \end{bmatrix} \tag{2.4}$$

The eigenvalues of the system of Eq. 2.3 are calculated by:

$$det\,(\lambda\mathbf{A} + \mathbf{B}) = \underline{\mathbf{0}} \tag{2.5}$$

Afterwards, for each eigenvalue λ_i, the corresponding eigenvector $\underline{\mathbf{\Phi_i}}$ is calculated as followed:

$$(\mathbf{A} - \lambda_i \mathbf{I}) \cdot \underline{\mathbf{\Phi_i}} = 0 \tag{2.6}$$

If the system of equations is speed independent (e.g. in the case where $\mathbf{G} = \mathbf{0}$), the eigenvalues and the eigenvectors are constant across the speed range of the engine. Nevertheless, mainly due to gyroscopic phenomena and speed dependent bearing coefficients, the eigenvalues change with the rotating speed of the engine. This phenomenon is depicted in Campbell diagram.

2.1.2 Unbalance Response Utilizing Linear Harmonic Analysis

Linear harmonic analysis is the method of calculating the forced response of the engine in the frequency domain. The unbalance force is usually the external force applied to the system and is described as followed:

$$\underline{\mathbf{f_u}} = \underline{\mathbf{f_m}} \cdot \cos(\Omega \cdot t + \theta_f) \tag{2.7}$$

$\underline{\mathbf{f_u}}$ is a force vector, thus each force can have a different magnitude $\underline{\mathbf{f_m}}$ and phase angle θ_f, but necessarily the same rotating speed Ω. The unbalance acts to specific degrees of freedom, so $\underline{\mathbf{f_u}}$ is generally a sparse vector.

The system of Eq. 2.1 is solved analytically as long as the matrices are not eccentricity dependent. In such manner, the system is linear and is solved separately for each rotating speed in the speed range of the engine. The solution provides the values of vector $\underline{\mathbf{x}}$, which are also harmonic functions of the same rotating speed:

$$\underline{\mathbf{x}} = \underline{\mathbf{x_m}} \cdot \cos(\Omega \cdot t + \theta_x) \tag{2.8}$$

Otherwise, if the system is nonlinear, it is necessary to resort to other methods in order to solve the equations in the frequency domain. One of these is the multi-harmonic method, presented later in the thesis.

2.1.3 Transient Response

There are many cases in which the solution of the system is not feasible in the frequency domain, e.g. non harmonic external forces or nonlinear systems. In these cases, the solution in the time domain is usually preferred.

Transient analysis calculates the response of the system over a period of time in which the engine runs up in its speed range. The response is calculated by numerical integration forward in time. The size of the time step is not constant for the whole speed range and varies depending on the system requirements. Also, the selection of the rotational acceleration is crucial. For large values, the effect of transient phenomena is important, yet small values lead to extremely time-consuming simulations.

Transient analysis is not generally preferred because it is significantly slower than linear harmonic analysis. However, transient analysis is the most suitable method for many problems, e.g. blade loss, rapid run-up, aircraft maneuvers [40].

If the system of Eq. 2.1 has dimension N, it can be also expressed as a first-order system of dimension 2N in state space by defining two new variables $\underline{\mathbf{x_1}} = \underline{\mathbf{x}}$ and $\underline{\mathbf{x_2}} = \dot{\underline{\mathbf{x}}}$. In this way, Eq. 2.1 is equivalent to the following system:

$$\begin{bmatrix} \dot{\underline{\mathbf{x_1}}} \\ \dot{\underline{\mathbf{x_2}}} \end{bmatrix} = \begin{bmatrix} \mathbf{0} & \mathbf{I} \\ -\mathbf{M^{-1}} \cdot \mathbf{K} & -\mathbf{M^{-1}} \cdot (\Omega \mathbf{G} + \mathbf{C}) \end{bmatrix} \cdot \begin{bmatrix} \underline{\mathbf{x_1}} \\ \underline{\mathbf{x_2}} \end{bmatrix} + \begin{bmatrix} \underline{\mathbf{0}} \\ -\mathbf{M^{-1}} \cdot \underline{\mathbf{f}} \end{bmatrix} \tag{2.9}$$

In transient analysis, the initial value problem of Eq. 2.9 is numerically integrated given an initial value $\begin{bmatrix} \underline{\mathbf{x_{1,0}}} \\ \underline{\mathbf{x_{2,0}}} \end{bmatrix}$. The solution is $\begin{bmatrix} \underline{\mathbf{x_1(t)}} \\ \underline{\mathbf{x_2(t)}} \end{bmatrix}$ at each time t.

2.2 Analytical Models for Squeeze Film Damper Forces

2.2.1 Basic Concepts

The cross-section of a rotor supported by a journal bearing is shown in Fig. 2.2. The radial clearance c_r is the difference between the internal diameter of the bearing R_b and the external diameter of the journal R_j. It is usually 500 to 1000 times smaller than R_b, but it is exaggerated in the figure. Bearing and journal centers are symbolized as O_b and O_j respectively. The difference between their position is the eccentricity e and the ratio $\epsilon = e/c_r$ is called eccentricity ratio. Its value ranges from 0 (for concentric bearing and journal) to 1 (when journal is in contact with the inner surface of the bearing).

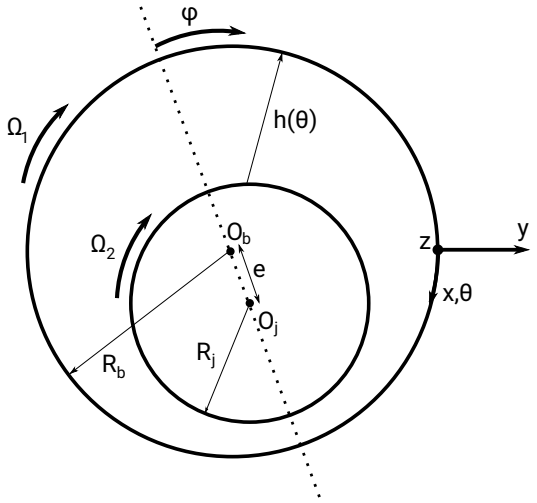

Figure 2.2: Basic kinematics of journal bearings

The small gap between the inner bearing surface and the outer journal surface is filled with lubrication oil, which is called oil film. When journal and bearing centers are not coincident, oil film thickness $h(\theta)$ varies in the circumferential direction. Its values range from $c_r - e$ to $c_r + e$. Angle θ counts from the positive y-axis to the direction of the rotational speed Ω_2. The profile of oil film thickness determines the profile of oil pressure and, finally, the total force exerted on the journal. This force is the main source of external damping in the rotor-bearing system.

Angle ϕ equals to 0 when oil film thickness is maximum and takes positive values in the direction of the journal rotation. Both angle θ and ϕ are defined with respect to the bearing center O_b, yet in different coordinate systems (fixed and rotating, respectively). Hence, the expression for film thickness h in the rotating system is:

$$h = c_r + e \cdot \cos\phi \tag{2.10}$$

In the range ϕ = (0,π), oil film thickness decreases and pressure is generated because of journal rotation (positive pressure in comparison to oil inlet pressure). This is called the wedge effect. On the other side, in the range = (π,2π) pressure is negative but its absolute value is relatively small.

2.2.2 Analytical Model for The Oil Flow in SFDs: Reynolds Equation

The Navier-Stokes equations describe the motion of a Newtonian fluid. For incompressible fluids (density ρ is constant), density derivative with respect to time equals to 0. Under the assumption of constant dynamic viscosity μ, the distribution of oil film pressure is calculated in all three dimensions by solving the following system of equations [39]:

$$\begin{aligned}
\frac{\partial u}{\partial x}+\frac{\partial v}{\partial y}+\frac{\partial w}{\partial z}&=0\\
\rho\left(\frac{\partial u}{\partial t}+u\cdot\frac{\partial u}{\partial x}+v\cdot\frac{\partial u}{\partial y}+w\cdot\frac{\partial u}{\partial z}\right)&=-\frac{\partial P}{\partial x}+\mu\left(\frac{\partial^2 u}{\partial x^2}+\frac{\partial^2 u}{\partial y^2}+\frac{\partial^2 u}{\partial z^2}\right)+\rho\cdot f_x\\
\rho\left(\frac{\partial v}{\partial t}+u\cdot\frac{\partial v}{\partial x}+v\cdot\frac{\partial v}{\partial y}+w\cdot\frac{\partial v}{\partial z}\right)&=-\frac{\partial P}{\partial y}+\mu\left(\frac{\partial^2 v}{\partial x^2}+\frac{\partial^2 v}{\partial y^2}+\frac{\partial^2 v}{\partial z^2}\right)+\rho\cdot f_y\\
\rho\left(\frac{\partial w}{\partial t}+u\cdot\frac{\partial w}{\partial x}+v\cdot\frac{\partial w}{\partial y}+w\cdot\frac{\partial w}{\partial z}\right)&=-\frac{\partial P}{\partial z}+\mu\left(\frac{\partial^2 w}{\partial x^2}+\frac{\partial^2 w}{\partial y^2}+\frac{\partial^2 w}{\partial z^2}\right)+\rho\cdot f_z
\end{aligned} \tag{2.11}$$

The last three equations are Navier-Stokes momentum equations in x (circumferential), y (radial) and z (axial) direction, respectively, and the first one is the continuity equation for incompressible fluids. f_x, f_y and f_z are components of the body force. Nevertheless, the system, in the form of Eq. 2.11, does not have an analytical solution, thus usually in practical applications a number of assumptions are made in order to simplify the equations.

In lubrication, oil film thickness is much smaller than the dimensions in axial and circumferential direction, thus the flow in the radial direction is neglected and many terms of the equation can be ignored. Eq. 2.11, in their nondimensional form, contain second-order terms in (c_r/R_j), which are neglected. Both acceleration and convective terms (left-hand side terms of momentum equations) can be ignored if Reynolds number is smaller than 500 (given that c_r/R_j equals at most to $1/500$). Reynolds number is defined based on the journal surface velocity u_2:

$$Re=\frac{\rho\cdot c_r\cdot u_2}{\mu} \tag{2.12}$$

Finally, body forces in the fluid film are neglected. Applying those assumptions, the system takes the following form:

$$\begin{aligned} \frac{\partial u}{\partial x} + \frac{\partial v}{\partial y} + \frac{\partial w}{\partial z} &= 0 \\ \frac{\partial P}{\partial x} &= \mu \cdot \frac{\partial^2 u}{\partial y^2} \\ \frac{\partial P}{\partial y} &= 0 \\ \frac{\partial P}{\partial z} &= \mu \cdot \frac{\partial^2 w}{\partial y^2} \end{aligned} \tag{2.13}$$

Hence, pressure is constant in the radial direction. Momentum equations in x and z direction can be integrated twice with respect to y. The boundary conditions for velocities u and w satisfy the no-slip condition between the oil and the solid bearing and journal surfaces:

- u = u_1, w = 0 at y = 0
- u = u_2, w = 0 at y = h

The integration leads to the following formulas for velocities u and w:

$$\begin{aligned} u = \frac{1}{2\mu} \cdot \frac{\partial P}{\partial x} \cdot y \cdot [y - h(\theta)] + \left[\frac{h(\theta) - y}{h(\theta)} \cdot u_1 + \frac{y}{h(\theta)} \cdot u_2 \right] \\ w = \frac{1}{2\mu} \cdot \frac{\partial P}{\partial z} \cdot y \cdot [y - h(\theta)] \,, \end{aligned} \tag{2.14}$$

where:

$$\theta = \frac{x}{R_b} \tag{2.15}$$

The expressions of Eq. 2.14 are substituted in the continuity equation, but the equation still contains two unknowns, v and P. By integrating (averaging) continuity equation in the radial direction, only v_1 and v_2, the values of radial velocity v for $y = 0$ and $y = h$, are needed for the derivation of Reynolds equation. This approximation is valid due to oil film thin geometry.

Finally, the Reynolds equation is obtained:

$$\frac{\partial}{\partial x}\left(\frac{h^3}{\mu} \cdot \frac{\partial P}{\partial x}\right) + \frac{\partial}{\partial z}\left(\frac{h^3}{\mu} \cdot \frac{\partial P}{\partial z}\right) = 6(u_1 - u_2) \cdot \frac{\partial h}{\partial x} + 6h \cdot \frac{\partial (u_1 + u_2)}{\partial x} + 12(v_2 - v_1) \tag{2.16}$$

The first term on the right-hand side is called ”wedge”, the second ”stretch” and the third ”squeeze”. In the wedge effect, pressure is increased when the fluid moves in

an oil film of decreasing thickness. In the stretch effect, pressure is generated when surface velocity varies in the circumferential direction. In the squeeze effect, pressure is increased due to changes of film thickness [18].

A more detailed approach for the derivation of Reynolds equation from continuity and Navier-Stokes equations can be found in [14], [31] and [39].

"Stretch", the second term on the right-hand side of the Reynolds equation, equals to 0. u_1 and u_2 are journal and bearing surface velocities, thus they are constant when both surfaces are rigid. Furthermore, "squeeze" term can be expressed as followed:

$$v_2 - v_1 = \frac{dh}{dt} \tag{2.17}$$

After some calculations, which are described in detail in [39], the form of the Reynolds equation is the following:

$$\frac{\partial}{\partial x}\left(\frac{h^3}{\mu}\cdot\frac{\partial P}{\partial x}\right) + \frac{\partial}{\partial z}\left(\frac{h^3}{\mu}\cdot\frac{\partial P}{\partial z}\right) = 6(u_1+u_2)\cdot\frac{\partial h}{\partial x} + 12\frac{\partial h}{\partial t} \tag{2.18}$$

Even in this simplified form, the Reynolds equation does not have an analytical solution, unless more approximations are considered. For significantly long bearings, with L/D ratio (length to diameter) over 1, the infinite length approximation is considered. This essentially means that the second term on the left-hand side of the Reynolds equation is neglected and it it is possible to be solved analytically. On the other side, for bearings with L/D less than 0.25 (or even less than 0.5), the short bearing approximation is considered and the first term on the left-hand side is neglected. Once more, the system can be solved analytically. Finally, for finite length bearings, that do not belong in the previous categories, it is necessary to solve the system numerically, using Finite Difference, Finite Volume or Finite Element Method [18].

Squeeze film dampers are usually designed to have L/D up to 0.2 in aerospace applications, therefore short bearing approximation provides highly accurate results in the calculations of the pressure distribution along the oil film. The Reynolds equation in rotating coordinates is considered:

$$\frac{\partial}{\partial z}\left(\frac{h^3}{\mu}\cdot\frac{\partial P}{\partial z}\right) = 6(\Omega_1+\Omega_2)\cdot\frac{\partial h}{\partial \theta} + 12\frac{\partial h}{\partial t} \tag{2.19}$$

Ω_1 and Ω_2 are the rotational speeds of the bearing and the journal, respectively, and equal the product of the corresponding surface velocity and radius.

2.2.3 Evaluation of SFD Impedance Forces

In the current Subsection, x and y represent a classic cartesian coordinate system. In order to solve the Eq. 2.19, it is assumed that the bearing is perfectly aligned. Thus, film

thickness h is not a function of the axial position z and is given by Eq. 2.10 in rotating coordinates and by 2.20 in fixed coordinates:

$$h = c_r - x \cdot \cos\theta - y \cdot \sin\theta \tag{2.20}$$

The right-hand side of the Eq. 2.19 is also not a function of z, therefore by integrating twice with respect to z, the Reynolds equation can be solved. The following boundary conditions are set at the two ends of the squeeze film damper:

- P(θ) = 0 at z = 0
- P(θ) = 0 at z = L

These boundary conditions apply for open-ended squeeze film dampers. However, there are other boundary conditions which are used for alternate seals configurations, e.g. end seals or piston rings.

The expression obtained for oil film pressure is the following:

$$P(\theta, z) = \frac{3\mu}{h^3} \cdot \left[(\Omega_1 + \Omega_2) \cdot \frac{\partial h}{\partial \theta} + 2\frac{\partial h}{\partial t} \right] \cdot (z^2 - Lz) \tag{2.21}$$

The Eq. 2.21 is the general expression for pressure and is applied for both journal bearings and squeeze film dampers. Nevertheless, the bearing and the journal are henceforth considered to be constrained from rotating (Ω_1 = Ω_2 = 0). Squeeze film dampers are usually located between the housing and the rolling element bearings, so their journals do not rotate, they only whirl. Moreover, film thickness is given by Eq. 2.20 in fixed coordinates and its derivative with respect to time is the following:

$$\frac{\partial h}{\partial t} = -\dot{x} \cdot \cos\theta - \dot{y} \cdot \sin\theta \tag{2.22}$$

The resulting expression for oil pressure is:

$$P(\theta, z) = \frac{6\mu}{h^3} \cdot [-\dot{x} \cdot \cos\theta - \dot{y} \cdot \sin\theta] \cdot (z^2 - L \cdot z) \tag{2.23}$$

Eq. 2.23 needs to be integrated in the circumferential and the axial direction to derive the expression for the oil film force in x and y direction:

$$\begin{aligned} F_x &= \int_0^L \int_0^{2\pi} P(\theta, z) \cdot \cos\theta \cdot R \, d\theta \, dz \\ F_y &= \int_0^L \int_0^{2\pi} P(\theta, z) \cdot \sin\theta \cdot R \, d\theta \, dz \end{aligned} \tag{2.24}$$

L and R are the symbols for SFD length and radius, respectively.

By substituting Eq. 2.23 and Eq. 2.20 in Eq. 2.24, film forces in x and y direction are the following:

$$\begin{aligned} F_x &= \mu \cdot R \cdot L^3 \int_0^{2\pi} \frac{\dot{x} \cdot \cos^2\theta + \dot{y} \cdot \sin\theta \cdot \cos\theta}{(c_r - x \cdot \cos\theta - y \cdot \sin\theta)^3}\, d\theta \\ F_y &= \mu \cdot R \cdot L^3 \int_0^{2\pi} \frac{\dot{x} \cdot \cos\theta \cdot \sin\theta + \dot{y} \cdot \sin^2\theta}{(c_r - x \cdot \cos\theta - y \cdot \sin\theta)^3}\, d\theta \end{aligned} \tag{2.25}$$

The expressions in Eq. 2.25 can only be integrated numerically. However, oil film forces can be expressed in the rotating coordinate system [10], be integrated using the formulas found in [11] and, finally, be expressed in the fixed coordinate system. This solution is faster because the numerical integration of Eq. 2.25 is not required.

Forces described in Eq. 2.25 are calculated without taking oil cavitation into account, hence the integration limits in the circumferential direction are 0 and 2π (full circle). This approach was first proposed by Sommerfeld in 1904 and allowed negative pressures of the oil film. In this case, the minimum negative pressure has the same absolute value as the maximum positive pressure. The results of the approach are accurate only for low bearing pressures.

In 1914, Gümbel was the first to include oil rupture in his model. In brief, he assumed that oil rupture arises near the minimum oil film thickness. Also, he proposed that the pressure remains equal to a constant value (P_{cav}) in the entire cavitated region. His approach takes into account only the positive pressures in half the oil film circumference (half-Sommerfeld or Gümbel condition) and it is valid for high bearing pressures.

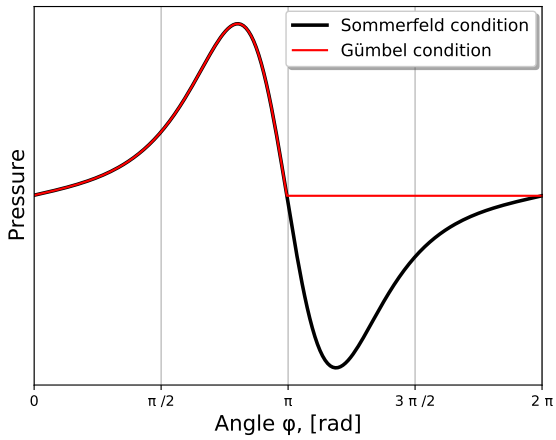

Figure 2.3: Pressure along the oil film circumference for Sommerfeld and Gümbel cavitation condition

More information about the phenomenon of cavitation and cavitation modeling for fluid film bearings are found in [12].

Gümbel's model is used henceforward for the calculations of the thesis. It is known that the pressure is positive only for half the oil film circumference, but the starting and ending angle of this range need to be calculated. The limits of the range of positive pressure depend on the velocities of the journal center $\dot{x}$ and $\dot{y}$. Considering Eq. 2.23, it is clear that $(z^2 - L \cdot z) < 0$ for $z = (0, L)$ and the film pressure is positive when:

$$P > 0 \Leftrightarrow \dot{x} \cdot \cos\theta + \dot{y} \cdot \sin\theta > 0 \tag{2.26}$$

Let:

$$\begin{aligned} \theta_1 &= atan2\,(-\dot{x}, \dot{y}) \\ \theta_2 &= \theta_1 + \pi \end{aligned} \tag{2.27}$$

The range of positive oil film pressure is (θ_1,θ_2).

Hence, the calculation of the oil film forces in x and y direction according to Gümbel's cavitation model is feasible using the integrals of Eq. 2.25 with integration limits (θ_1,θ_2).

The final expressions for the oil film forces are the following:

$$\begin{aligned} F_x &= \mu \cdot R \cdot L^3 \int_{\theta_1}^{\theta_2} \frac{\dot{x} \cdot \cos^2\theta + \dot{y} \cdot \sin\theta \cdot \cos\theta}{(c_r - x \cdot \cos\theta - y \cdot \sin\theta)^3}\, d\theta \\ F_y &= \mu \cdot R \cdot L^3 \int_{\theta_1}^{\theta_2} \frac{\dot{x} \cdot \cos\theta \cdot \sin\theta + \dot{y} \cdot \sin^2\theta}{(c_r - x \cdot \cos\theta - y \cdot \sin\theta)^3}\, d\theta \end{aligned} \tag{2.28}$$

It is now obvious that the forces depend on both the position and the velocity of the journal center.

They can be included in the equations concerning the journal displacements in x and y direction as followed:

$$\begin{aligned} m_i \cdot \ddot{\boldsymbol{x}} + (\Omega g_i + c_i) \cdot \dot{\boldsymbol{x}} + k_i \cdot \boldsymbol{x} &= -F_x \\ m_{i+1} \cdot \ddot{\boldsymbol{x}} + (\Omega g_{i+1} + c_{i+1}) \cdot \dot{\boldsymbol{x}} + k_{i+1} \cdot \boldsymbol{x} &= -F_y, \end{aligned} \tag{2.29}$$

where m_i is the i^{th} row of mass matrix, c_{i+1} is the $(i+1)^{th}$ row of damping matrix etc.

Some characteristic cases are examined in order to calculate the oil film forces along the orbit. The first two cases are circular orbits with small and large eccentricity about the bearing center. Subsequently, elliptic orbits about the bearing center and circular and elliptic orbits about off-centered points are considered. The geometric characteristics of the orbits are described in detail in Table 2.1.

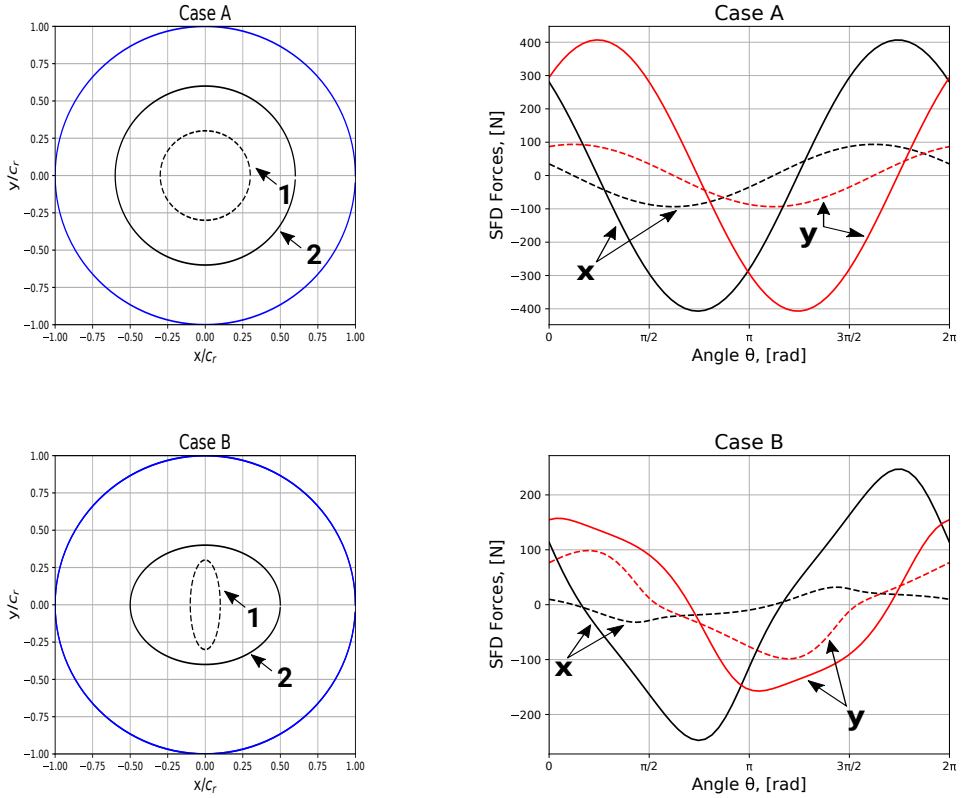

Figure 2.4: SFD forces on circular and elliptic orbits about the bearing center

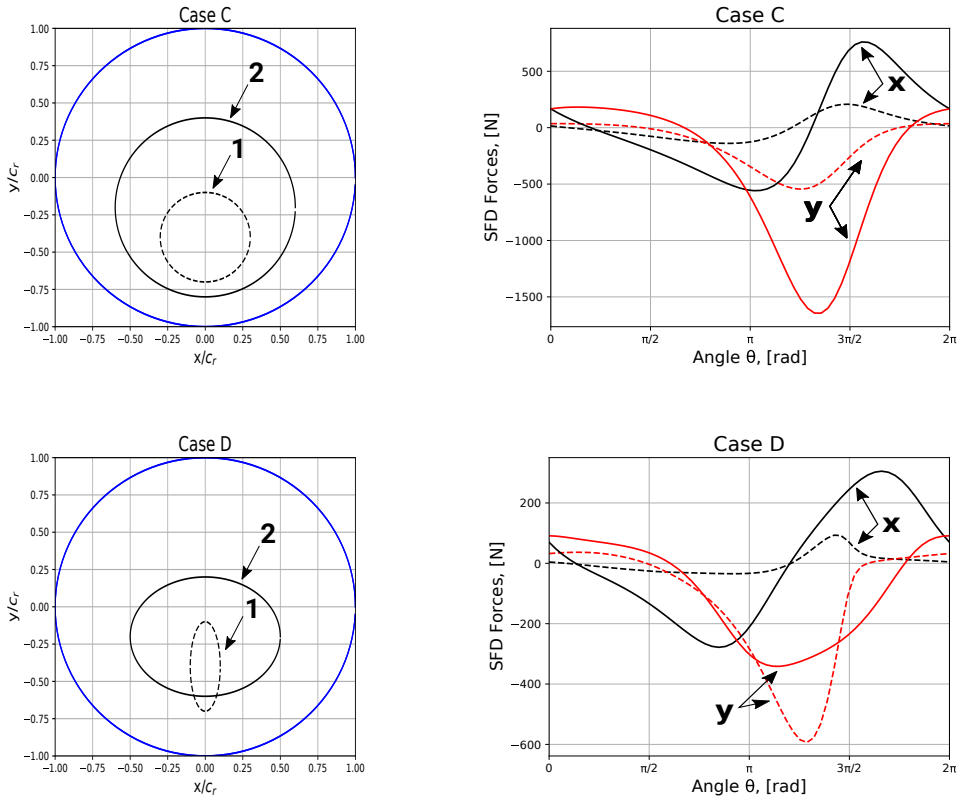

Figure 2.5: SFD forces on circular and elliptic orbits about off-centered points

Table 2.1: Cases for the evaluation of oil film forces along the journal orbit

Case	Semi-x-axis/c_r	Semi-y-axis/c_r	Orbit center/c_r
A-1	0.3	0.3	(0,0)
A-2	0.6	0.6	(0,0)
B-1	0.1	0.3	(0,0)
B-2	0.5	0.4	(0,0)
C-1	0.3	0.3	(0,-0.4)
C-2	0.6	0.6	(0,-0.2)
D-1	0.1	0.3	(0,-0.4)
D-2	0.5	0.4	(0,-0.2)

The forces are calculated for the following parameters:

- Dynamic viscosity $\mu = 2.5$ mPas
- SFD diameter $D = 160$ mm
- SFD length $L = 20$ mm
- SFD radial clearance $c_r = 100$ μm
- Whirling speed $\omega = 1000$ rad/s

The most important conclusions from Fig. 2.4 and 2.5 are the following:

- Large eccentricities result in large force amplitudes.
- For circular orbits about the center, the forces in both x and y direction can be described by expressions like $A \cdot cos(\omega \cdot t + \phi_c)$ or $A \cdot sin(\omega \cdot t + \phi_s)$. This means that F_x and F_y are phase shifted sine or cosine functions of amplitude A.
- For elliptic orbits about the center, both forces have zero mean value and their minimum negative is equal to the maximum positive value.
- For both circular and elliptic orbits about the bearing center, oil firm forces equal to 0 at two angles ϕ_1 and ϕ_2 that always satisfy the following relation:

$$\phi_2 = \phi_1 + \pi \tag{2.30}$$

- An orbit about (x_0,y_0) where x_0,$y_0 \neq 0$ generates forces with nonzero mean value.

The figures of the present Subsection are an important example in order to understand the great variety of oil film forces exerted by squeeze film dampers, both in shape along the journal orbit and magnitude. For this reason, in many cases, the modeling of SFDs as linear elements is not a valid approximation and may provide completely inaccurate results.

The formulas of Eq. 2.28 can also be expressed as:

$$
\begin{aligned}
F_x &= c_{xx}(x, y, \dot{x}, \dot{y}) \cdot \dot{x} + c_{xy}(x, y, \dot{x}, \dot{y}) \cdot \dot{y} \\
F_y &= c_{yx}(x, y, \dot{x}, \dot{y}) \cdot \dot{x} + c_{yy}(x, y, \dot{x}, \dot{y}) \cdot \dot{y},
\end{aligned}
\tag{2.31}
$$

where:

$$
c_{xx} = \mu R L^3 \int_{\theta_1}^{\theta_2} \frac{\cos^2\theta}{(c_r - x \cdot \cos\theta - y \cdot \sin\theta)^3}\, d\theta \quad , \quad c_{yy} = \mu R L^3 \int_{\theta_1}^{\theta_2} \frac{\sin^2\theta}{(c_r - x \cdot \cos\theta - y \cdot \sin\theta)^3}\, d\theta
$$

$$
c_{xy} = c_{yx} = \mu R L^3 \int_{\theta_1}^{\theta_2} \frac{\sin\theta \cdot \cos\theta}{(c_r - x \cdot \cos\theta - y \cdot \sin\theta)^3}\, d\theta
\tag{2.32}
$$

It is necessary to examine the effect of the journal position on SFD nonlinear damping coefficients. Sommerfeld cavitation condition is considered in order to make the coefficients velocity independent. The results are presented in Fig. 2.6.

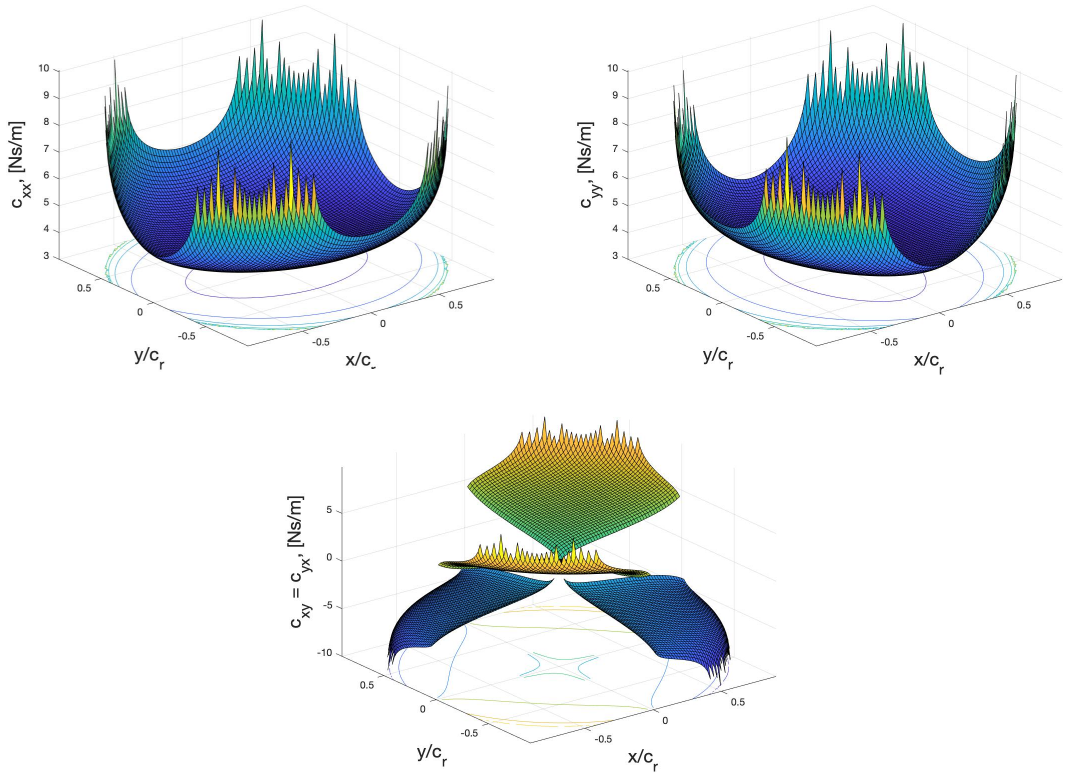

Figure 2.6: SFD nonlinear damping coefficients for Sommerfeld cavitation condition

The common logarithm of SFD coefficients is reflected across the z-axis. Direct coefficients c_{xx} and c_{yy} have always positive values in contrast with cross-coupled coefficients c_{xy} and c_{yx}. The influence of journal position on all four coefficients is clear since their

order of magnitude varies significantly. As expected, the largest coefficients are observed for high eccentricities.

Subsequently, the effect of both journal velocity and displacement is investigated. The results for circular orbits about the centerline are displayed in Fig. 2.7.

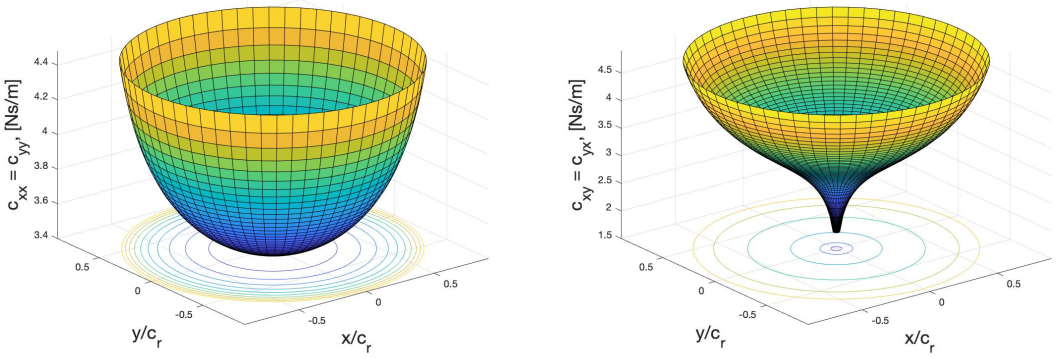

Figure 2.7: SFD nonlinear damping coefficients along circular orbits about the centerline for Gümbel cavitation condition

The common logarithm of SFD coefficients is reflected across the z-axis. Because of orbit symmetry about the bearing center, direct coefficients c_{xx} and c_{yy} are equal to each other. The same applies to cross-coupled coefficients c_{xy} and c_{yx}. Moreover, it is observed that all coefficients are constant along the circular orbit. Direct coefficients vary from 2500 to 25000 N·s/m and cross-coupled coefficients from 35 to 31500 N·s/m.

Similarly to Eq. 2.28, Capone [13] derives some analytical expressions for the nonlinear oil film forces, which give the exact same results. The forces are calculated based on the short bearing approximation and depend on the geometry of the squeeze film damper (length, diameter, radial clearance), the oil viscosity, the whirling speed of the journal, the position and the velocity of the journal center.

2.2.4 SFD Force Coefficients for Specific Cases

Barrett and Gunter also calculated expressions for the oil film forces in [10]. Moreover, they examined the case of circular orbits of radius e around the bearing center and derived analytical expressions for the oil film forces in rotating coordinates:

$$\begin{aligned} F_r &= \frac{2\mu \cdot R \cdot L^3 \cdot \epsilon \cdot \omega}{c_r^3 \cdot (1-\epsilon^2)^2} \cdot e = k_0 \cdot e \\ F_\theta &= \frac{\mu \cdot R \cdot L^3 \cdot \pi}{2c_r^3 \cdot (1-\epsilon^2)^{3/2}} \cdot e \cdot \omega = c_0 \cdot (e \cdot \omega) \end{aligned} \tag{2.33}$$

ω is the journal whirling speed. k_0 is a nonlinear stiffness coefficient and its product with the journal eccentricity e gives the radial force that acts as the centripetal force along the

circular orbit. c_0 is a nonlinear damping coefficient. The tangential force is calculated by multiplying c_0 and the journal velocity which equals to e $\cdot\omega$ for circular orbits.

Expressions for the oil film forces in the cartesian coordinate system are derived combining Eq. 2.33 and Eq. 2.34.

$$\begin{aligned} F_x &= F_r \cdot \cos\theta - F_t \cdot \sin\theta \\ F_y &= F_r \cdot \sin\theta + F_t \cdot \cos\theta \end{aligned} \tag{2.34}$$

Only for circular orbits about centerline, journal velocities and positions are related as followed:

$$\begin{aligned} \dot{x} &= -\omega \cdot y \\ \dot{y} &= \omega \cdot x \end{aligned} \tag{2.35}$$

Finally, it can be deduced from Eq. 2.34 and 2.35 that the nonlinear stiffness and damping coefficients k_0 and c_0 of the cylindrical coordinate system can also be used in the cartesian coordinate system:

$$\begin{aligned} F_x &= c_0 \cdot \dot{x} + k_0 \cdot x = c_0 \cdot \dot{x} + \frac{k_0}{\omega} \cdot \dot{y} \\ F_y &= c_0 \cdot \dot{y} + k_0 \cdot y = -\frac{k_0}{\omega} \cdot \dot{x} + c_0 \cdot \dot{y} \end{aligned} \tag{2.36}$$

The coefficients of Eq. 2.36 depend on the eccentricity, thus they are constant along circular orbits. The same conclusion is drawn from Fig. 2.7.

Squeeze film dampers do not really produce stiffness. A static eccentricity does not generate any oil flow and, as a result, no force acts on the journal. In fact, only in the presence of journal velocity, SFD exerts force on the journal. However, in the case of circular orbits about the bearing center, the cross-coupled damping coefficients can be replaced with the stiffness coefficient k_0 because of Eq. 2.35.

Moreover, San Andrés [5] calculates analytical coefficients for some special cases. He considers the following form of Reynolds equation in cylindrical coordinates:

$$\frac{1}{R} \cdot \frac{\partial}{\partial\theta}\left(h^3 \cdot \frac{\partial P}{\partial\theta}\right) + \frac{\partial}{\partial z}\left(h^3 \cdot \frac{\partial}{\partial z}\right) = 12\mu \cdot \frac{\partial h}{\partial t} + \rho \cdot h^2 \cdot \frac{\partial^2 h}{\partial t^2} \tag{2.37}$$

and derives damping and mass coefficients for small amplitude perturbations about an off-centered point and for both Sommerfeld's and Gümbel's cavitation model. He considers a short length open-ended squeeze film damper. The coefficients are functions of the static journal eccentricity.

The forces of Eq. 2.28 do not depend on the journal acceleration. This is because the second term of the right-hand side of Eq. 2.37 was neglected in the Reynolds equation.

This term is also the source of the mass coefficients derived by San Andrés. The mass coefficients are only valid for small SFD Reynolds numbers and, specifically:

$$Re_{SFD} = \frac{\rho \cdot \omega \cdot c_r^2}{\mu} < 10 \tag{2.38}$$

He also calculates constant damping and mass coefficients for orbits of small ampitude ($< 0.25 c_r$) and for finite length open-ended SFD in [4].

2.3 Discrete Fourier Transform (DFT)

2.3.1 Basics

At each angle ϕ_i, the position and velocity of the journal center are known. The substitution of these values in Eq. 2.28 and the integration with limits θ_1 to θ_2 results in the values of the oil film forces F_x and F_y for each angle ϕ_i. Hence, for ϕ ranging from 0 to 2π, the forces are calculated along the orbit, as in Fig. 2.4 and 2.5.

Oil film forces are calculated discretely in a finite number of points, assuming P, along the orbit and the angle interval between two consecutive points is $\Delta\theta$. The forces are periodic with period $T = 2\pi/\omega$ (ω is the whirling frequency of the journal).

Only for the case of circular orbits about the bearing center, the forces are harmonic functions of the angle ϕ. Otherwise, the forces along the orbit cannot be described accurately by a single sine or cosine function.

Therefore, in order to precisely approximate the oil film forces, higher order harmonics need to be taken into account. Hence, the forces can be expanded using the following general expression:

$$F = \overline{F} + \sum_{n=1}^{\infty} [c_n \cdot \cos(n\phi + \phi_n)] = \overline{F} + c_1 \cdot \cos(\phi + \phi_1) + \cdots + c_N \cdot \cos(N\phi + \phi_N) + \cdots , \tag{2.39}$$

where $\overline{F}$ is the mean value of the force F along the orbit.

Eq. 2.39 describes an infinite series of trigonometric functions. In practical application, the number of orders N is finite and varies depending on the case. For instance, for circular orbits about the bearing center, only the first order is required. Thus, the approximative expression is the following:

$$F \approxeq \overline{F} + \sum_{n=1}^{N} [c_n \cdot \cos(n\phi + \phi_n)] = \overline{F} + c_1 \cdot \cos(\phi + \phi_1) + \cdots + c_N \cdot \cos(N\phi + \phi_N) \tag{2.40}$$

The mean value $\overline{F}$ is calculated by:

$$\overline{F} = \frac{1}{P} \cdot \sum_{i=0}^{P-1} F(\phi_i) \tag{2.41}$$

Each order's term can be replaced by:

$$c_n \cdot \cos(n\phi + \phi_n) = c_{n1} \cdot \sin(n\phi) + c_{n2} \cdot \cos(n\phi) \tag{2.42}$$

Discrete Fourier Transform is used in order to determine the values of the force amplitudes c_n and phase angles ϕ_n. A complex number X_n is calculated for every order n from [19]:

$$X_n = \frac{2}{P} \sum_{i=0}^{P-1} F(\phi_i) \cdot e^{-j \cdot n \cdot \phi_i} \tag{2.43}$$

Eq. 2.44 express the relation between the complex number X_n and the two real numbers c_n and ϕ_n:

$$\begin{aligned} c_n &= |X_n| = \sqrt{Re(X_n)^2 + Im(X_n)^2} \\ \phi_n &= \underline{/X_n} = atan2\left(Im(X_n), Re(X_n)\right) \end{aligned} \tag{2.44}$$

Consequently, if the number of orders are defined, it is very simple to calculate approximative expressions for oil film forces using DFT. This expression is always a sum of cosine or sine functions of the defined orders.

The Discrete Fourier Transforms X_1 of a cosine and a sine signal of amplitude 1 equals to 1 and -j, respectively.

2.3.2 Application of DFT on SFD Forces

In the current Subsection, characteristic cases are examined in order to determine the number of harmonics needed to satisfactorily approximate the oil film forces along the orbit.

As mentioned above, for circular orbits about the bearing center, SFD forces are harmonic functions, synchronous to the whirling motion of the journal. Consequently, only the first-order harmonic is required in order to estimate perfectly the forces. The magnitude of higher-order harmonics DFT $|X_n|$, n = 2,3,$\cdots$, equals to 0.

For the case of circular orbit of radius $0.6c_r$ about the bearing center, oil film forces in x and y direction, as well as the DFT approximative forces, are presented in Fig. 2.8. As expected, the forces are identical.

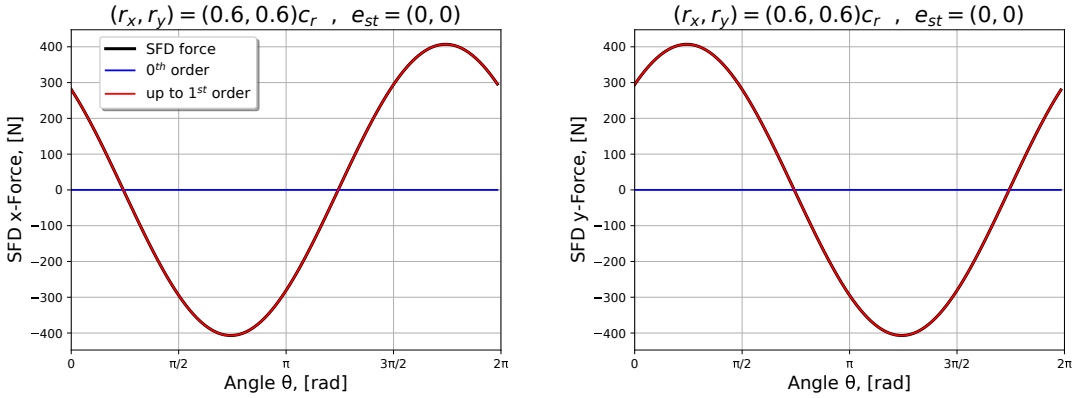

Figure 2.8: Approximation of oil film forces using DFT on circular centered orbits

For orbits about the bearing center, the mean value $\overline{F}$ of oil film force always equals to 0. Furthermore, the force in each direction equals to 0 at two angles ϕ_1 and ϕ_2. The angular distance between ϕ_1 and ϕ_2 is always π radians. In this case, SFD force is described by an odd function, namely it satisfies the following relations:

$$F(\phi + \phi_1) = -F(-\phi + \phi_1)\ ,\ F(\phi + \phi_2) = -F(-\phi + \phi_2) \tag{2.45}$$

Due to these relations, the magnitude of even-order harmonics DFT equals to 0. Hence, only odd-order harmonics are considered.

The approximation of SFD forces for elliptic orbit with semi-minor-axis $0.1c_r$ (parallel to x-axis) and semi-major-axis $0.3c_r$ (parallel to y-axis) about the bearing center is presented in Fig. 2.9.

Each higher-order harmonic improves both the magnitude and the phase angle of the approximative force. The first-order harmonic is not sufficient to approximate the real force, however third-order harmonic upgrades remarkably the results. Generally, the improvements in the approximation of SFD forces decrease as higher-orders harmonics are introduced. The relative difference between the amplitude of the real and the approximative force (using the first 7 harmonics) is about 1%.

Finally, for circular orbits of static eccentricity $e_{st} = (x_0, 0)$ or $(0, y_0)$, the mean value of the force in x and y direction, respectively, equals to 0. Nevertheless, in every orbit about an off-centered point, namely circular or elliptic orbit about (x_0, y_0), no symmetry is observed. Hence, no harmonics can be omitted.

The approximation of SFD forces for elliptic orbit with semi-major-axis $0.5c_r$ (parallel to x-axis) and semi-minor-axis $0.4c_r$ (parallel to y-axis) about $(0, -0.2)c_r$ is presented in Fig. 2.10.

Exceptional results are observed using the first 4 harmonics. In this case, the relative error of the approximation is less than 1%. It is also important to notice the nonzero mean value of the real force in y direction.

The remarks of the present Subsection are very useful since the user is capable to predefine the orders that are necessary for the approximation of the response and make the software presented in Chapter 3 significantly faster.

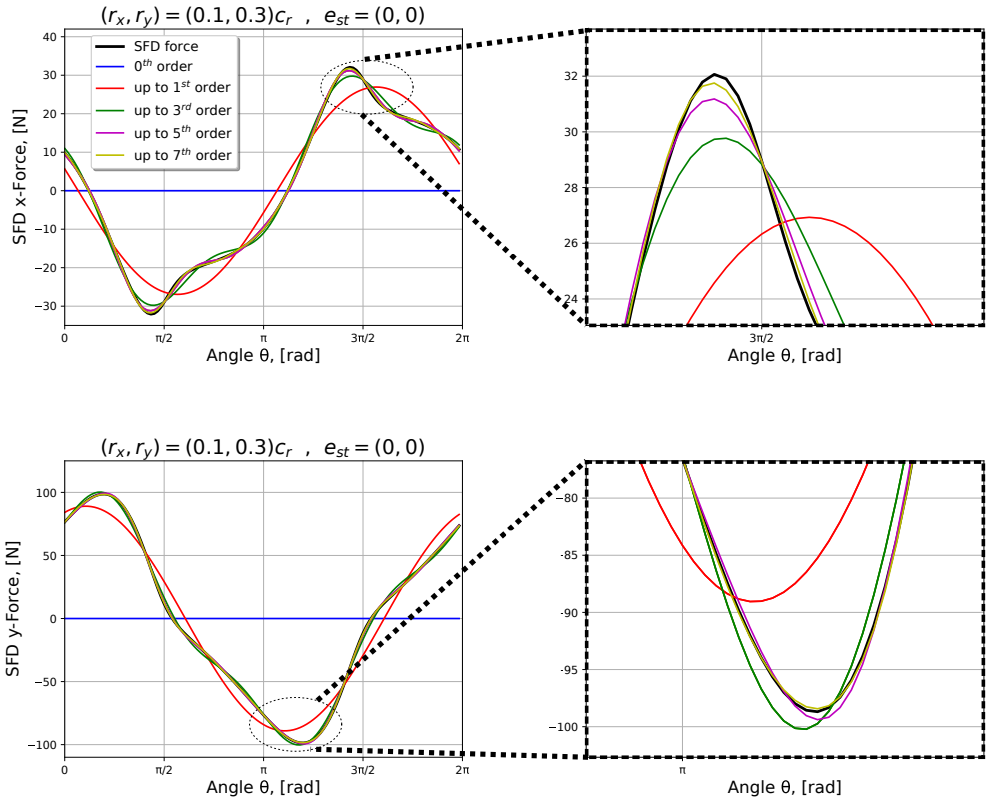

Figure 2.9: Approximation of oil film forces using DFT on elliptic centered orbits (detail view included)

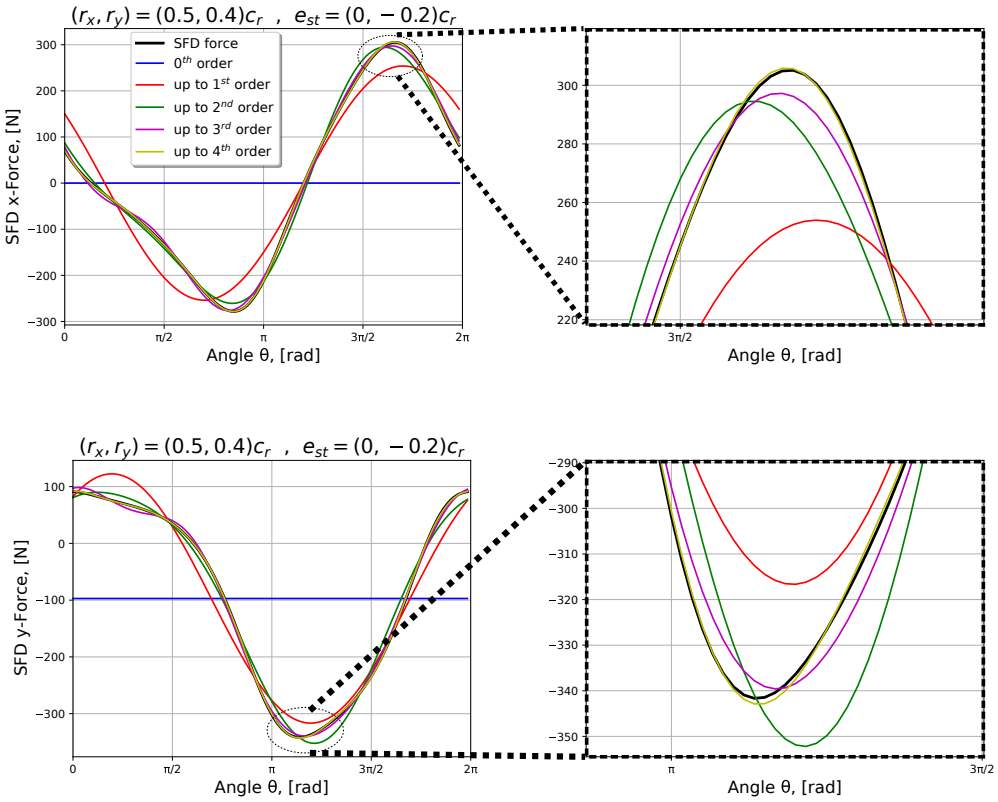

Figure 2.10: Approximation of oil film forces using DFT on elliptic off-centered orbits (detail view included)

2.4 Mono-Harmonic Analysis

A dynamic system governed by a system of equations of the following form is considered:

$$\mathbf{M} \cdot \underline{\ddot{\mathbf{x}}} + (\Omega\mathbf{G} + \mathbf{C}) \cdot \underline{\dot{\mathbf{x}}} + \mathbf{K} \cdot \underline{\mathbf{x}} = \underline{\mathbf{f_u}} + \underline{\mathbf{f_b}} \,, \tag{2.46}$$

where $\underline{\mathbf{f_u}}$ is the mass unbalance force and $\underline{\mathbf{f_b}}$ is the force exerted by the bearings.

In the current Section, the unbalance response is calculated using the method of linear harmonic analysis. The system of Eq. 2.46 is solved separately at each rotational speed of the engine and the values of vector $\underline{\mathbf{x}}$ are defined.

If there are nonlinear bearings supporting the engine, their forces are linearized by considering them to be proportional to the rotor eccentricity and its derivatives:

$$\underline{\mathbf{f_b}} = -\mathbf{M_b} \cdot \underline{\ddot{\mathbf{x}}} + -\mathbf{C_b} \cdot \underline{\dot{\mathbf{x}}} - \mathbf{K_b} \cdot \underline{\mathbf{x}} \tag{2.47}$$

Hence, constant bearing mass, damping and stiffness matrices are introduced in the system of equations:

$$\mathbf{M_{tot}} \cdot \underline{\ddot{\mathbf{x}}} + (\Omega\mathbf{G} + \mathbf{C_{tot}}) \cdot \underline{\dot{\mathbf{x}}} + \mathbf{K_{tot}} \cdot \underline{\mathbf{x}} = \underline{\mathbf{f}} \,, \tag{2.48}$$

where:

$$\mathbf{M_{tot}} = \mathbf{M} + \mathbf{M_b} \quad , \quad \mathbf{C_{tot}} = \mathbf{C} + \mathbf{C_b} \quad , \quad \mathbf{K_{tot}} = \mathbf{K} + \mathbf{K_b} \tag{2.49}$$

Moreover, if matrices $\mathbf{M}$, $\mathbf{G}$, $\mathbf{C}$, $\mathbf{K}$ are constant, the system of Eq. 2.48 is a nonhomogenous linear system of ordinary differential equations. Therefore, an analytical solution using linear harmonic analysis is feasible.

Since the system of equations is linearized and the unbalance force is the only external force, which is harmonic and synchronous to the rotational speed of the engine, the solution of the system is also harmonic and synchronous to the rotational speed.

Let the rotating frequency of the aircraft engine be Ω. The unbalance force vector $\underline{\mathbf{f_u}}$ is described by:

$$\underline{\mathbf{f_u}} = \underline{\mathbf{f_m}} \cdot e^{j\Omega \cdot t} \tag{2.50}$$

The vector $\underline{\mathbf{f_m}}$ is constant, thus the vector $\underline{\mathbf{f_u}}$ is periodic with period T=1/Ω. As a result, the solution vector $\underline{\mathbf{x}}$ has the general form:

$$\underline{\mathbf{x}} = \underline{\mathbf{x_m}} \cdot e^{j\Omega \cdot t} \,, \tag{2.51}$$

where $\underline{\mathbf{x_m}}$ is a constant vector.

The first two derivatives of vector $\underline{\mathbf{x}}$ with respect to time are:

$$\begin{aligned} \dot{\underline{\mathbf{x}}} &= j\underline{\mathbf{x_m}}\Omega \cdot e^{j\Omega \cdot t} \\ \ddot{\underline{\mathbf{x}}} &= -\underline{\mathbf{x_m}}\Omega^2 \cdot e^{j\Omega \cdot t} \end{aligned} \tag{2.52}$$

The substitution of Eq. 2.52 to Eq. 2.48 leads to:

$$[-\Omega^2\mathbf{M_{tot}} + j\Omega\left(\Omega\mathbf{G} + \mathbf{C_{tot}}\right) + \mathbf{K_{tot}}] \cdot \underline{\mathbf{x_m}}e^{j\Omega \cdot t} = \underline{\mathbf{f_m}}e^{j\Omega \cdot t} \tag{2.53}$$

Damping decribed by $\mathbf{C}$ is viscous, therefore proportional to velocity. On the other hand, structural damping is proportional to displacement, thus it can be modeled as stiffness. However, it must be an imaginary stiffness term in order to provide damping when it is multiplied by displacement [35]. The structural damping of the engine is included in the solution of the system in frequency domain as followed:

$$[-\Omega^2\mathbf{M_{tot}} + j\Omega\left(\Omega\mathbf{G} + \mathbf{C_{tot}}\right) + \mathbf{K_{tot}} + j\mathbf{C_{str}}] \cdot \underline{\mathbf{x_m}}e^{j\Omega \cdot t} = \underline{\mathbf{f_m}}e^{j\Omega \cdot t} \tag{2.54}$$

The matrix on the left-hand side of Eq. 2.54 is called dynamic stiffness $\mathbf{K_{dyn}}$:

$$\mathbf{K_{dyn}} = -\Omega^2\mathbf{M_{tot}} + j\Omega\left(\Omega\mathbf{G} + \mathbf{C_{tot}}\right) + \mathbf{K_{tot}} + j\mathbf{C_{str}} \tag{2.55}$$

The nontrivial solution of Eq. 2.53 and 2.54 is calculated by:

$$\underline{\mathbf{x_m}} = \mathbf{K_{dyn}}^{-1} \cdot \underline{\mathbf{f_m}} \tag{2.56}$$

Combining Eq. 2.51 and Eq. 2.56:

$$\underline{\mathbf{x}} = \mathbf{K_{dyn}}^{-1} \cdot \underline{\mathbf{f_m}}e^{j\Omega \cdot t} \tag{2.57}$$

2.5 Multi-Harmonic Analysis

Multi-harmonic analysis is an extension of the linear harmonic analysis. In some cases, nonlinear bearings cannot be linearized as in Eq. 2.47.

The linearized forces exerted by bearings on rotors and casings can be added to the system of 2.46 in two ways. The first one is on the right-hand side as an external force (in addition to the unbalance force) and the second one is on the left-hand side as mass,

damping and stiffness coefficients. The first way requires significantly simpler calculations, thus it is preferred henceforth.

With the addition of nonlinear squeeze film dampers, the system of equations is the following:

$$\mathbf{M} \cdot \underline{\ddot{\mathbf{x}}} + (\Omega \mathbf{G} + \mathbf{C}) \cdot \underline{\dot{\mathbf{x}}} + \mathbf{K} \cdot \underline{\mathbf{x}} = \underline{\mathbf{f_u}} + \underline{\mathbf{f_{SFD}}} \tag{2.58}$$

It is supposed that the forces exerted by the rest of the bearings are linear and are included in the matrices of the left-hand side.

In Section 2.3, approximative expressions for oil film forces were derived using Discrete Fourier Transform. These expressions can substitute $\underline{\mathbf{f_{SFD}}}$ in the Right-Hand Side (RHS) of Eq. 2.58. Supposing that $\underline{\mathbf{f_{SFD}}}$ consists of terms of 0^{th}, 1^{st}, 2^{nd}, $\cdots$, N^{th} order, the right-hand side of Eq. 2.58 is also a sum of terms of 0^{th}, 1^{st}, 2^{nd}, $\cdots$, N^{th} order:

$$RHS = \underline{\mathbf{f_u}} + \underline{\mathbf{f_{SFD}}} = \underline{\mathbf{f_0}} + (\underline{\mathbf{f_m}} + \underline{\mathbf{f_1}})e^{j\Omega \cdot t} + \underline{\mathbf{f_2}} e^{2j\Omega \cdot t} + \cdots + \underline{\mathbf{f_N}} e^{Nj\Omega \cdot t} \tag{2.59}$$

Hence, the left-hand side of Eq. 2.58 has to be a sum of 1^{st} to N^{th}-order terms too. The solution vector $\underline{\mathbf{x}}$ now has the following general form:

$$\underline{\mathbf{x}} = \underline{\mathbf{x_0}} + \underline{\mathbf{x_1}} e^{j\Omega \cdot t} + \underline{\mathbf{x_2}} e^{2j\Omega \cdot t} + \cdots + \underline{\mathbf{x_N}} e^{Nj\Omega \cdot t} \tag{2.60}$$

The first two derivatives of $\underline{\mathbf{x}}$ with respect to time are now:

$$\begin{aligned} \underline{\dot{\mathbf{x}}} &= j\underline{\mathbf{x_1}}\Omega \cdot e^{j\Omega \cdot t} + 2j\underline{\mathbf{x_2}}\Omega \cdot e^{2j\Omega \cdot t} + \cdots + Nj\underline{\mathbf{x_N}}\Omega \cdot e^{Nj\Omega \cdot t} \\ \underline{\ddot{\mathbf{x}}} &= -\underline{\mathbf{x_1}}\Omega^2 \cdot e^{j\Omega \cdot t} + -4\underline{\mathbf{x_2}}\Omega^2 \cdot e^{2j\Omega \cdot t} + \cdots + -N^2\underline{\mathbf{x_N}}\Omega^2 \cdot e^{Nj\Omega \cdot t} \end{aligned} \tag{2.61}$$

The substitution of expressions of Eq. 2.59-2.61 to Eq. 2.58 results in the following system of equations:

$$\underline{\mathbf{h_0}} + \underline{\mathbf{h_1}} e^{j\Omega \cdot t} + \cdots + \underline{\mathbf{h_N}} e^{Nj\Omega \cdot t} = \underline{\mathbf{f_0}} + (\underline{\mathbf{f_m}} + \underline{\mathbf{f_1}})e^{j\Omega \cdot t} + \cdots + \underline{\mathbf{f_N}} e^{Nj\Omega \cdot t} \ , \tag{2.62}$$

where:

$$\begin{aligned} \underline{\mathbf{h_0}} &= \mathbf{K} \cdot \underline{\mathbf{x_0}} \\ \underline{\mathbf{h_1}} &= \left[-\Omega^2 \mathbf{M} + j\Omega \left(\Omega \mathbf{G} + \mathbf{C} \right) + \mathbf{K} \right] \cdot \underline{\mathbf{x_1}} \\ \underline{\mathbf{h_n}} &= \left[-n^2 \cdot \Omega^2 \mathbf{M} + jn \cdot \Omega \left(\Omega \mathbf{G} + \mathbf{C} \right) + \mathbf{K} \right] \cdot \underline{\mathbf{x_n}} \ , \end{aligned} \tag{2.63}$$

for n = 2, 3, $\cdots$, N.

The system of Eq. 2.62 is valid for every time t, if the following equations apply:

$$\begin{aligned} \underline{\mathbf{h_0}} &= \underline{\mathbf{f_0}} \\ \underline{\mathbf{h_1}} &= \underline{\mathbf{f_m}} + \underline{\mathbf{f_1}} \\ \underline{\mathbf{h_n}} &= \underline{\mathbf{f_n}} \, , \end{aligned} \tag{2.64}$$

for n = 2, 3, $\cdots$, N.

Hence:

$$\begin{aligned} \underline{\mathbf{x_0}} &= \mathbf{K}^{-1} \cdot \underline{\mathbf{f_0}} \\ \underline{\mathbf{x_1}} &= \left[-\mathbf{M} \cdot \Omega^2 + j \left(\Omega \mathbf{G} + \mathbf{C} \right) \cdot \Omega + \mathbf{K} \right]^{-1} \cdot \left(\underline{\mathbf{f_m}} + \underline{\mathbf{f_1}} \right) \\ \underline{\mathbf{x_n}} &= \left[-n^2 \mathbf{M} \cdot \Omega^2 + nj \left(\Omega \mathbf{G} + \mathbf{C} \right) \cdot \Omega + \mathbf{K} \right]^{-1} \cdot \underline{\mathbf{f_n}} \end{aligned} \tag{2.65}$$

2.6 Definition of Unbalance Excitation

Consider a shaft rotating at a speed Ω and a lumped mass m which is located at a distance e from the shaft axis of rotation. Mass unbalance force $\underline{\overrightarrow{\mathbf{f_u}}}$ is produced and acts as a centrifugal force:

$$\underline{\overrightarrow{\mathbf{f_u}}} = \left(m \cdot e \cdot \Omega^2 \right) \underline{\overrightarrow{\mathbf{r}}}, \tag{2.66}$$

where $\underline{\overrightarrow{\mathbf{r}}}$ is the unit vector of the radial direction.

Rotor vibrations are caused by unbalance forces. They mainly originate from errors in the manufacturing process, thermal deformation, material lack of homogeneity, wear and corrosion [19].

According to International Standard ISO 1940/1 [1], the maximum permissible unbalance value is specified by the balance quality grades. In this way, the balance quality requirements are classified for various types of machinery in different G quality grades.

Rotors of the same type have the same permissible residual unbalance U_{per}, which is proportional to the rotor mass m. The permissible residual specific unbalance e_{per} is defined as the ratio of U_{per} over m. Also, e_{per} is inversely proportional to the service speed of the rotor and rotors of the same type have the same $e_{per} \cdot \Omega$. All in all, U_{per} is a function of the service speed, the G quality grade and the rotor mass.

For an aircraft engine and its rotors, balance grades G2.5 and G6.3 are usually used. U_{per} is calculated from graphs included in ISO 1940/1 or from the following relation:

$$U_{per} = 9549 G \cdot \frac{m}{\Omega}, \tag{2.67}$$

where G is the selected balance quality grade (in mm/s), m is the rotor weight (in kg) and Ω is the service speed (in RPM). In this way U_{per} is calculated in g·mm units.

For the simulations of the present thesis, two unbalance cases are applied:

- In the case of **static unbalance**, two unbalances of the same magnitude and phase angle are considered.
- In the case of **dynamic unbalance**, two unbalances of the same magnitude and 180° phase angle difference are considered.

For static unbalance, the forces $\underline{\mathbf{f_{u1}}}$ and $\underline{\mathbf{f_{u2}}}$ in x and y direction are calculated by:

$$\underline{\mathbf{f_u}} = \underline{\mathbf{f_{u1}}} = \underline{\mathbf{f_{u2}}} = \begin{bmatrix} f_{u,x} \\ f_{u,y} \end{bmatrix} = \begin{bmatrix} \frac{U_{per}}{2} \cdot \Omega^2 \\ -j\frac{U_{per}}{2} \cdot \Omega^2 \end{bmatrix} \cdot e^{j\Omega \cdot t} \tag{2.68}$$

The unbalance force in y direction has a phase lag of 90° when compared to the force in x direction.

For dynamic unbalance, the forces $\underline{\mathbf{f_{u1}}}$ and $\underline{\mathbf{f_{u2}}}$ in x and y direction are given by:

$$\begin{aligned} \underline{\mathbf{f_{u1}}} &= \begin{bmatrix} f_{u1,x} \\ f_{u1,y} \end{bmatrix} = \begin{bmatrix} \frac{U_{per}}{2} \cdot \Omega^2 \\ -j\frac{U_{per}}{2} \cdot \Omega^2 \end{bmatrix} \cdot e^{j\Omega \cdot t} \\ \underline{\mathbf{f_{u2}}} &= \begin{bmatrix} f_{u2,x} \\ f_{u2,y} \end{bmatrix} = \begin{bmatrix} -\frac{U_{per}}{2} \cdot \Omega^2 \\ j\frac{U_{per}}{2} \cdot \Omega^2 \end{bmatrix} \cdot e^{j\Omega \cdot t} \end{aligned} \tag{2.69}$$

The two unbalance forces have a phase difference of 180° in each direction.

3 The Multi-Harmonic Method for The Evaluation of Dynamic Response on Jeffcott Rotor

3.1 Linear Jeffcott Rotor Model with 4 Degrees of Freedom

In the present Section, a Jeffcott rotor of diameter D supported by two linear bearings B_1 and B_2 is considered. The model is taken from [40]. The rotor revolves with speed Ω and consists of a massless shaft and a disk attached to it. The Young's modulus and the density of the rotor are symbolized by E and ρ, respectively. Its total mass m_d is concentrated on the disk, which is located in half the distance L between the bearings. The rotor-bearing configuration is presented in Fig. 3.1:

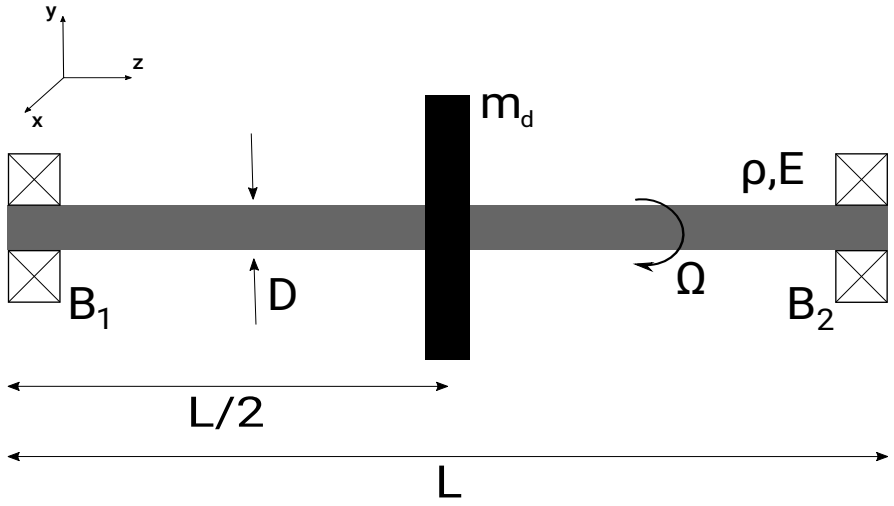

Figure 3.1: Jeffcott rotor supported by two bearings

3.1.1 Equations of Motion

Each bearing is modeled as a mass (m_b) - spring (k_b) - damper (c_b) system. The mass m_b is the mass of the journal and no additional mass (due to the presence of bearings) is introduced to the system. Bearing total stiffness k_b comes from both the bearing itself and the squirrel cage, while total damping c_b comes from the bearing and the squeeze film damper. The bearings are connected to the housing, which is modeled as rigid ground. The shaft stiffness is symbolized by k_s and its damping equals to zero. Mass

unbalance force F_u acts on the disk and the gravitational force is not taken into account in the calculations. Eventually, the system is simplified in the following model (same for x and y direction):

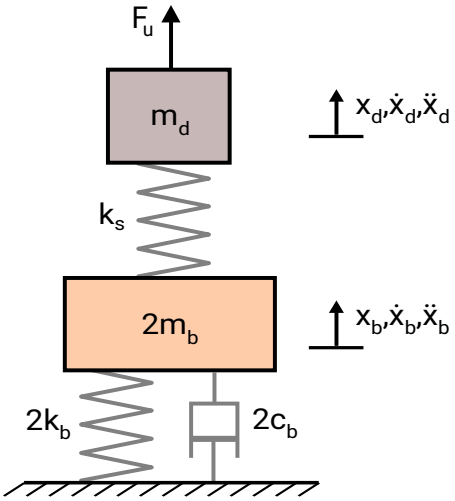

Figure 3.2: Simplified model of the Jeffcott rotor

The degrees of freedom of the disk are x_d and y_d. Since the system is symmetric, the bearings respond in the same manner. Hence, the same set of degrees of freedom (x_b and y_b) is used to describe both bearings' response. Moreover, their mass, damping and stiffness are parallel to each other, thus they are added together (e.g $m_{b,tot} = 2m_b$).

Angular displacements are not considered in the current system. Furthermore, x and y direction are not coupled. Therefore, the equations of motion for the disk and journal mass in x and y direction are the following:

$$\begin{aligned} m_d \cdot \ddot{x}_d + k_s \cdot (x_d - x_b) &= m_d \cdot e \cdot \Omega^2 \cdot e^{j\Omega \cdot t} \\ m_d \cdot \ddot{y}_d + k_s \cdot (y_d - y_b) &= -j m_d \cdot e \cdot \Omega^2 \cdot e^{j\Omega \cdot t} \\ 2m_b \cdot \ddot{x}_b + k_s \cdot (x_b - x_b) + 2k_b \cdot x_b + 2c_b \cdot \dot{x}_b &= 0 \\ 2m_b \cdot \ddot{y}_b + k_s \cdot (y_b - y_d) + 2k_b \cdot y_b + 2c_b \cdot \dot{y}_b &= 0 \end{aligned} \tag{3.1}$$

The shaft stiffness k_s is calculated by:

$$k_s = \frac{48E \cdot I}{L^3} = \frac{3E \cdot \pi \cdot D^4}{4L^3} \tag{3.2}$$

The Eq. 3.1 are also described by the system of Eq. 3.3:

$$\mathbf{M} \cdot \underline{\ddot{\mathbf{x}}} + \mathbf{C} \cdot \underline{\dot{\mathbf{x}}} + \mathbf{K} \cdot \underline{\mathbf{x}} = \underline{\mathbf{f_u}} \ , \tag{3.3}$$

where:

$$\mathbf{M} = \begin{bmatrix} m_d & 0 & 0 & 0 \\ 0 & m_d & 0 & 0 \\ 0 & 0 & 2m_b & 0 \\ 0 & 0 & 0 & 2m_b \end{bmatrix} \quad , \quad \mathbf{K} = \begin{bmatrix} k_s & 0 & -k_s & 0 \\ 0 & k_s & 0 & -k_s \\ -k_s & 0 & k_s + 2k_b & 0 \\ 0 & -k_s & 0 & k_s + 2k_b \end{bmatrix}$$
$$\mathbf{C} = \begin{bmatrix} 0 & 0 & 0 & 0 \\ 0 & 0 & 0 & 0 \\ 0 & 0 & 2c_b & 0 \\ 0 & 0 & 0 & 2c_b \end{bmatrix} \quad , \quad \underline{\mathbf{f_u}} = \begin{bmatrix} m_d \cdot e \cdot \Omega^2 \cdot e^{j\Omega \cdot t} \\ -jm_d \cdot e \cdot \Omega^2 \cdot e^{j\Omega \cdot t} \\ 0 \\ 0 \end{bmatrix} \quad , \quad \underline{\mathbf{x}} = \begin{bmatrix} x_d \\ y_d \\ x_b \\ y_b \end{bmatrix} \tag{3.4}$$

No gyroscopic phenomena are observed because the disk is located exactly at half the distance between the two bearings.

Consequently, at each rotational speed Ω, vector $\underline{\mathbf{x}}$, which contains all 4 degrees of freedom, is calculated analytically by:

$$\underline{\mathbf{x}} = (-\Omega^2\mathbf{M} + j\Omega\mathbf{C} + \mathbf{K})^{-1} \cdot \underline{\mathbf{f_u}} \tag{3.5}$$

In the case of speed dependent bearing stiffness and damping coefficients, the solution of the system is given by:

$$\underline{\mathbf{x}} = [-\Omega^2\mathbf{M} + j\Omega\mathbf{C}(\Omega) + \mathbf{K}(\Omega)]^{-1} \cdot \underline{\mathbf{f_u}} \tag{3.6}$$

3.1.2 Linear Dynamic Model: Constant and Speed Dependent Bearing Coefficients

The goal of the present Subsection is the investigation of the effects of speed dependent bearings on the dynamic behaviour of the system. The following values are considered for the parameters of the system: disk mass 100 kg, journal mass 10 kg, shaft stiffness 10^8 N/m, speed range (0,30000) RPM and eccentricity 10^{-5} m. The stiffness and the damping of the bearings range between 50 and 150% or 25 and 175% of the constant values. In total, the cases of Table 3.1 are examined.

In cases involving variable coefficients, the minimum value is observed for zero rotational speed and the maximum for 30000 RPM. The coefficients at every other speed are calculated using linear interpolation.

Using Eq. 2.5, the Campbell diagram is calculated for each case and is presented in Fig. 3.3.

Only forward whirling (FW) natural frequencies are considered for the Campbell diagram. For the system of constant coefficients, the critical speeds are 6692 RPM and 27068

Table 3.1: Cases for the evaluation of the influence of speed dependent bearing coefficients

Case	Bearing stiffness	Bearing damping
1	k_b	c_b
2	$(0.5k_b, 1.5k_b)$	c_b
3	$(0.25k_b, 1.75k_b)$	c_b
4	k_b	$(0.5c_b, 1.5c_b)$
5	k_b	$(0.25c_b, 1.75c_b)$

RPM. Both stiffness and damping have a major influence on the second eigenfrequency. In particular, stiffness moves the critical speed to a higher value and damping to a lower value. Overall, their effect on the eigenfrequencies of the system is very important and cannot be ignored.

The unbalance response of the disk is also examined for the cases of Table 3.1. The results are depicted in Fig. 3.4.

The results of unbalance response agree with Campbell diagram concerning the first critical speed, since the resonance is observed at 6692 RPM. The resonance of the second critical speed is not visible. Moreover, lower damping values lead to larger and narrow amplitudes and lower stiffness values lead to lower amplitudes.

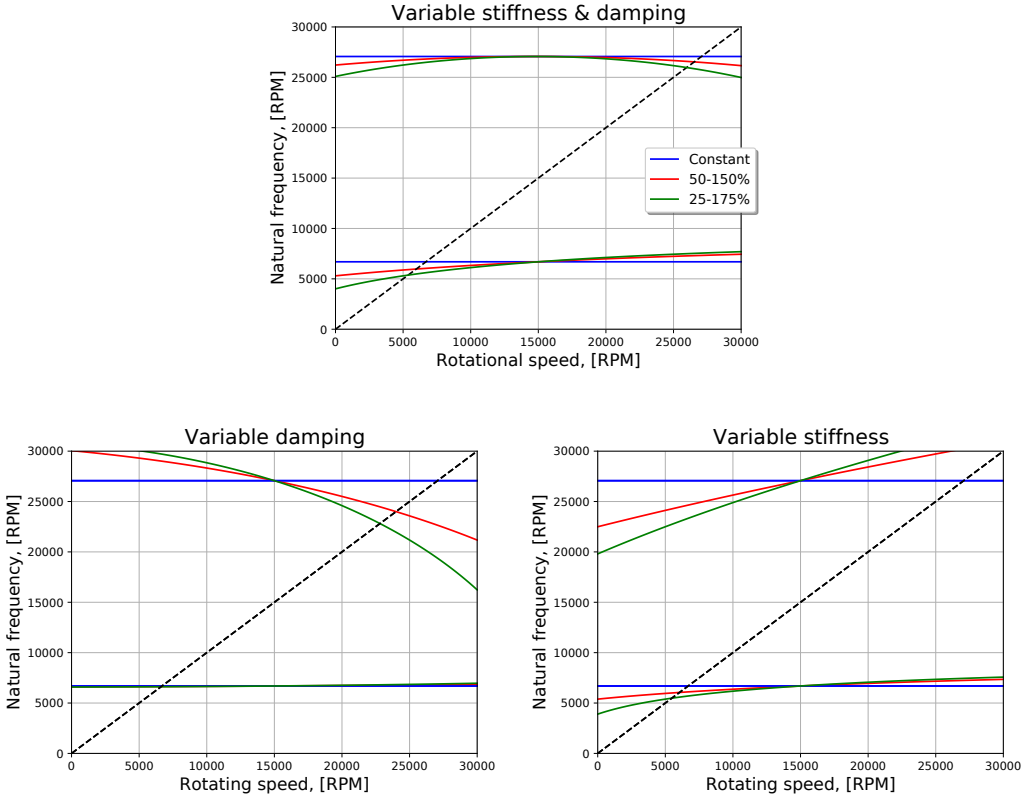

Figure 3.3: Effect of variable stiffness and damping coefficients on natural frequencies

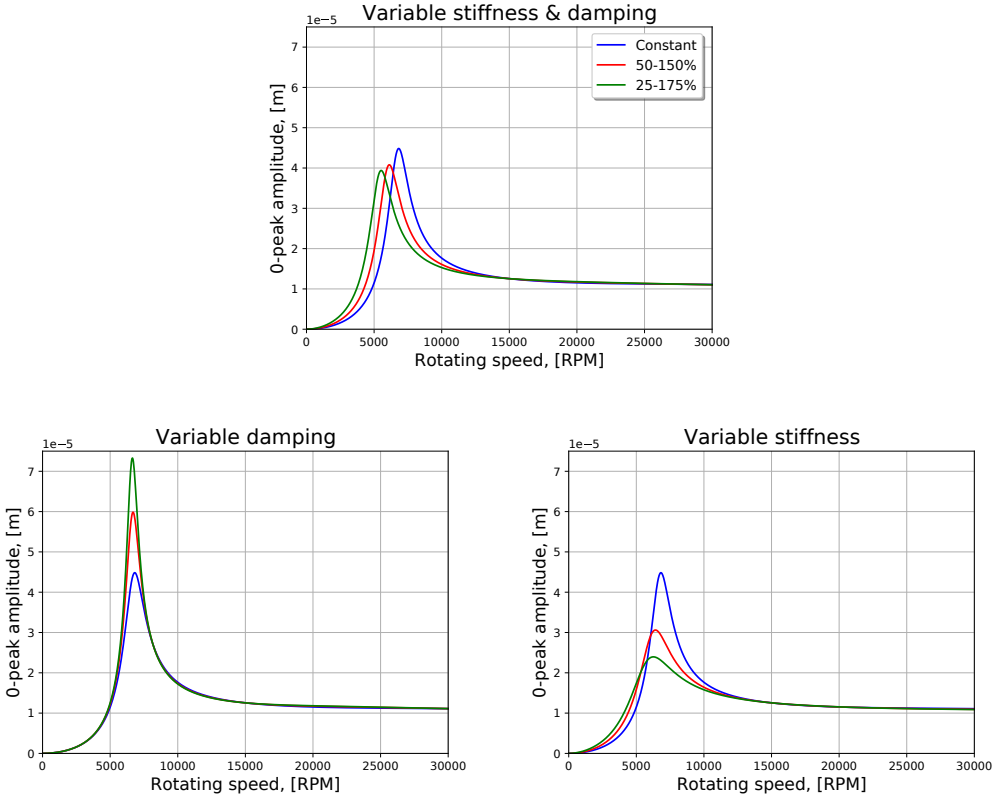

Figure 3.4: Effect of variable stiffness and damping coefficients on unbalance response

The results of linear harmonic analysis (using bearing damping that ranges from 65% to 135% of a typical bearing damping value) are provided. Afterwards, they are compared to the results of transient analysis (using the analytical SFD forces). The goal is to examine if, using constant coefficients, the achieved accuracy is sufficient. The results are presented in Fig. 3.5.

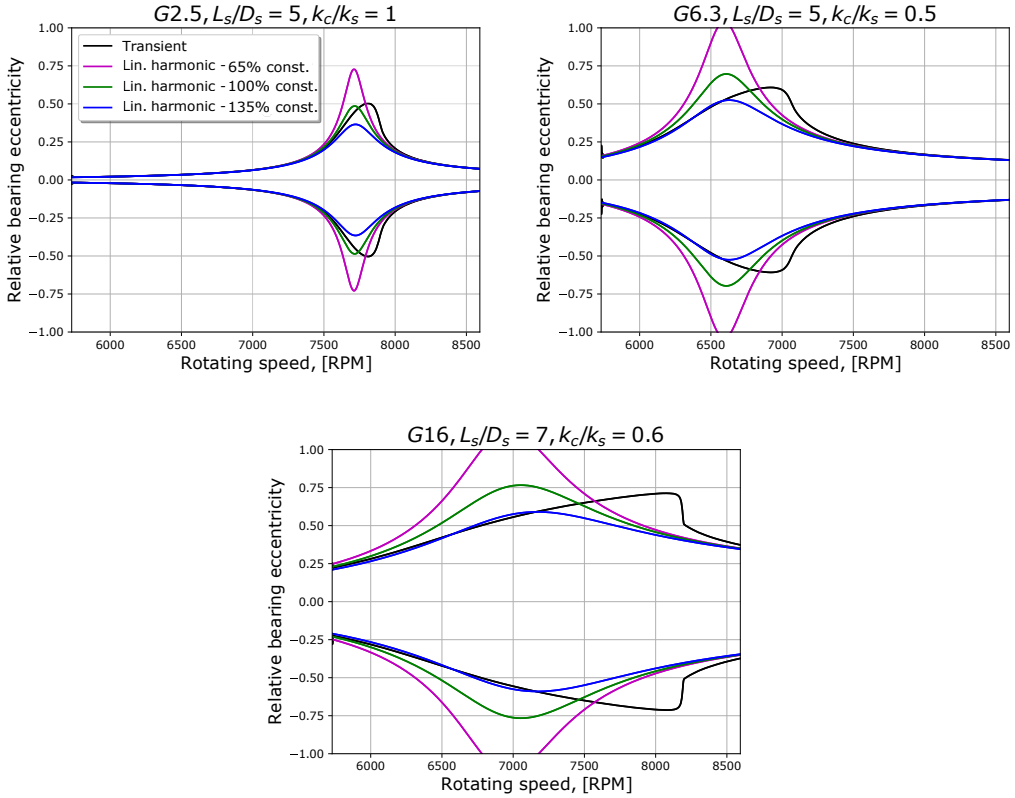

Figure 3.5: Comparison of the unbalance response with constant coefficients to the transient response

Although, in some cases, the results of linear harmonic analysis (using the typical bearing damping value) approximate decently the amplitude of the journal motion, they fail to predict the critical speed and, mainly, the shape of the amplitude. Actually, the shapes provided by analysis with constant coefficients are always symmetric and it is impossible to approximate shapes like the ones presented in Fig. 3.5.

However, due to its low computational cost, linear harmonic analysis is a useful tool that can be used in combination with more advanced methods, such as the multi-harmonic method that is presented in detail in the next Section.

Specifically, it is possible to use it as a predictive tool. Since it is possible to locate all the resonances of the speed range in a few seconds, even with a large error, the more accurate method can be used only around the resonances and the rest of the response can be calculated from linear harmonic analysis with constant coefficients. Observing Fig. 3.5, it is clear that the response is approximated well in rotating speeds far from resonances.

3.2 Introduction of Nonlinear SFDs in The Rotor System

The next step is the introduction of nonlinear bearings or squeeze film dampers to the simple system examined in Section 3.1. The effects caused by the rotor and bearings weight are also taken into account in some simulations of the present Section.

The forces exerted by nonlinear bearings are a function of solution vector $\underline{\mathbf{x}}$ and its derivatives. Actually, the bearing displacement and velocity in x and y direction have a substantial effect on oil film forces, as discussed in the Chapter 2. For this reason, squeeze film dampers are not modeled as linear elements for the following rotor dynamic simulations.

Generally, $\underline{\mathbf{x}}$ is a complex vector that represents the magnitude and the phase angle of the four degrees of freedom in the system. However, if the external forces are represented by a series of N harmonics, $\underline{\mathbf{x}}$ gives the magnitude and the phase angle of each harmonic and each DoF. In this case, the size of complex vector $\underline{\mathbf{x}}$ is 4N.

By supposing initial values for the N harmonics of the four DoFs (symbolized by vectors $\underline{\mathbf{x}_\mathbf{d}^0}$, $\underline{\mathbf{y}_\mathbf{d}^0}$, $\underline{\mathbf{x}_\mathbf{b}^0}$ and $\underline{\mathbf{y}_\mathbf{b}^0}$), the journal orbit can be computed (at P discrete points). Each one of the four vectors has size N and all together consist $\underline{\mathbf{x}^0}$. The number of points P is user-defined and needs to be large enough in order to sufficiently approximate the motion of the journal, yet below some limits for time-efficiency purposes.

Having calculated the orbit, the values of SFD forces are given by Eq. 2.28 (also at P points along the orbit). Afterwards, Discrete Fourier Transform is applied and the forces are approximated by a series of N harmonics of the rotational speed (see Eq. 2.40).

The rearrangement of Eq. 2.65 leads to the following expression:

$$\begin{aligned} \underline{\mathbf{g_1}} &= \left[-\mathbf{M}\cdot\Omega^2 + j\left(\Omega\mathbf{G}+\mathbf{C}\right)\cdot\Omega+\mathbf{K}\right]\cdot\underline{\mathbf{x_1}} - \left(\underline{\mathbf{f_m}}+\underline{\mathbf{f_1}}\right) = \underline{\mathbf{0}} \\ \underline{\mathbf{g_n}} &= \left[-n^2\mathbf{M}\cdot\Omega^2 + nj\left(\Omega\mathbf{G}+\mathbf{C}\right)\cdot\Omega+\mathbf{K}\right]\cdot\underline{\mathbf{x_n}} - \underline{\mathbf{f_n}} = \underline{\mathbf{0}}\,, \end{aligned} \tag{3.7}$$

where n = 2, 3, $\cdots$, N.

The matrices $\mathbf{M}$, $\mathbf{G}$, $\mathbf{C}$, $\mathbf{K}$ and the vector $\underline{\mathbf{f_m}}$ are constant and the magnitudes of SFD forces $\underline{\mathbf{f_n}}$, n = 1, $\cdots$, N, are calculated by Eq. 2.40 based on the initially hypothesized values $\underline{\mathbf{x}_\mathbf{b}^0}$ and $\underline{\mathbf{y}_\mathbf{b}^0}$. Therefore, the values of $\underline{\mathbf{g_n}}$, n = 1, $\cdots$, N, are evaluated.

A new vector $\underline{\mathbf{x^1}}$ is calculated as a function of the old vector $\underline{\mathbf{x}^0}$, the values of $\underline{\mathbf{g_n}}$ and the first derivatives of $\underline{\mathbf{g_n}}$ with respect to $\underline{\mathbf{x}}$ evaluated at $\underline{\mathbf{x}^0}$. These derivatives are included in the Jacobian matrix of dimensions 4N by 4N. The relative difference between $\underline{\mathbf{x^1}}$ and $\underline{\mathbf{x}^0}$ is evaluated. If the difference is large, the computations are repeated, starting the new iteration of the algorithm from the vector $\underline{\mathbf{x^1}}$. This procedure continues until two consecutive values of vector $\underline{\mathbf{x}}$, $\underline{\mathbf{x^{k-1}}}$ and $\underline{\mathbf{x^k}}$, have a negligible relative difference. The relative difference is calculated at each iteration by the following formula (given for the r^{th} element of $\underline{\mathbf{x}}$):

$$\delta_r^i = \left| \frac{x_r^i - x_r^{i-1}}{x_r^{i-1}} \right| \quad , \quad x_r^{i-1} \neq 0 \, , \tag{3.8}$$

where δ_r^i is the relative difference calculated after the i^{th} iteration. It is highlighted that the exponents are used to represent the number of the current iteration and not the exponential function.

The desired relative difference is selected by the user. Convergence is achieved when the calculated relative difference is smaller than the desired one.

Undoubtedly, there is a possibility that the algorithm does not converge after a large number of iterations. This happens mainly for cases of high eccentricity (close to radial clearance c_r and, typically, larger than 0.9-0.95c_r), where the derivatives of nonlinear forces with respect to eccentricity are extremely large. However these cases are not of great importance since the roughness of outer ring surface plays an important role in the friction conditions and Reynolds equation no longer applies. Therefore, another model is required in these cases.

In general, the maximum number of function calls is decided by the user and must be defined according to the number of degrees of freedom in the system since there is a strong relation between the two quantities (more Jacobian evaluations for large systems).

The calculations of each frequency are initialized taking into account the solutions of the previous frequencies. If the program does not converge in the specified number of iterations, the calculations start over from a low estimated value (of order 1%c_r). This is very common in the cases of jump phenomena, since the requested solution is fairly far from the estimated one (based on the solutions of previous frequencies).

The algorithm explained above is depicted in the flowchart of Fig. 3.6.

The validity of the multi-harmonic method is investigated by comparing its results to the results of transient analysis in Section 3.4. The algorithm of Fig. 3.6, as well as the rest of the software developed for the current thesis, are implemented in *Python*.

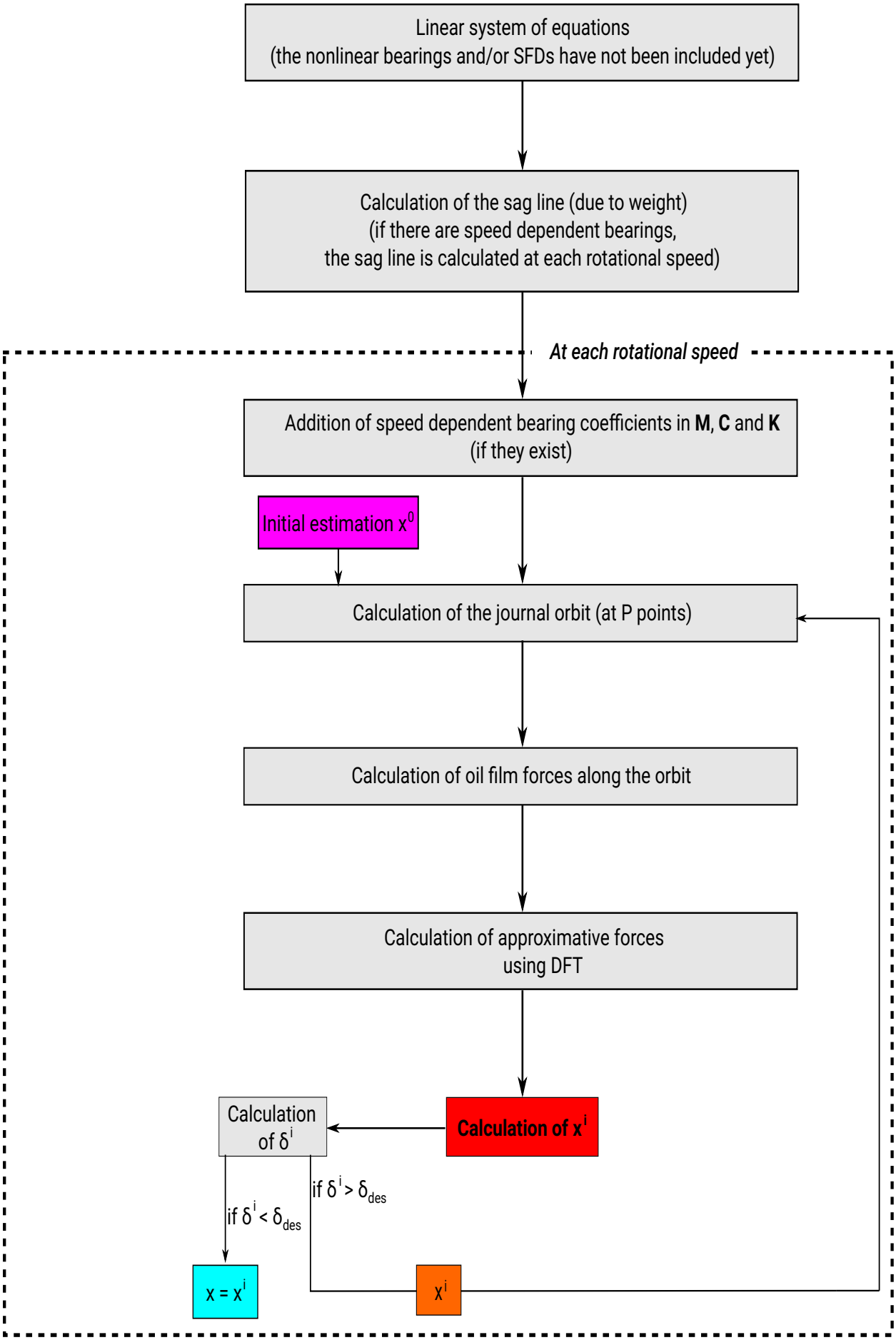

Figure 3.6: Flowchart for the calculation of the unbalance response using the multi-harmonic method

3.3 Numerical Solution of The Dynamic System

Before presenting the results of the method described in Section 3.2, it is necessary to briefly refer to the numerical procedures applied and the software used in the current thesis.

3.3.1 Software

Different types of rotordynamics simulations were conducted with MTU in-house tools. Their results were used as a reference for the results produced with the software developed for the present thesis. All jet engine models, from the simple FEM Jeffcott rotor to the realistic aircraft engine model, were realized with MTU's in-house tool. The tools were also employed for linear rotor dynamic analysis, such as modal analysis and linear harmonic analysis. The same results were also provided from *OpenAERAS*, another MTU in-house software. Moreover, *OpenAERAS* was used for the extraction of mass **M**, gyroscopic **G**, damping **C** and stiffness **K** matrices of the models.

As mentioned already, all the software developed for the thesis is implemented in *Python*. Finally, *MSC Nastran* was employed for the calculation of FEM Jeffcott rotor transient response.

3.3.2 Root-Finding Methods

The system of N nonlinear equations presented in Eq. 3.7 needs to be solved numerically. There is a plethora of root-finding methods in the bibliography concerning numerical methods, e.g. Jacobi, Gauss-Seidel and Newton-Raphson methods. Furthermore, the majority of these methods are implemented in programming languages, such as *Python*.

SciPy is an open-source *Python* library that contains tools used for scientific calculations. Numerical integration routines, DFT tools, interpolation and optimization algorithms are only a few of the tools contained in *SciPy* library.

SciPy.optimize provides routines for optimization (minimizing or maximizing objective functions), root-finding (linear or nonlinear equations), curve-fitting and least squares problems.

A multidimensional root-finding routine is necessary for the calculations of the current thesis. *SciPy.optimize* offers over 10 suitable routines, such as *root* and *fsolve*. *root* is a routine that contains 10 different methods for the calculation of the solution of nonlinear systems. Many of these methods are implemented in independent routines, e.g. *broyden1* and *anderson*.

For the purposes of the current thesis, *fsolve* is mainly used. The method *lm* of *root* routine has also been tested for a small number of simulations. However, it is considered to provide results similar to *fsolve*. The maximum relative error (difference) *xtol*, the maximum number of calls to the function *nfev* and the starting estimate for the roots *x0*

are defined for every simulation. Furthermore, there are many parameters concerning the Jacobian matrix. A user-defined function *fprime* can be used in order to calculate the derivatives of g_n, n = 1, $\cdots$, N, from Eq. 3.7 across the rows of the matrix. See [33] for more details about the possible inputs of the routine).

3.3.3 Initial Value Estimation at New Frequencies

A crucial topic for root-finding algorithms is the selection of the initial value $\underline{\mathbf{x}^0}$ (*x0* in *Python*). In fact, the selected initial value may define the convergence or not of the software. Hence, in the present Subsection, a method to calculate an initial estimation $\underline{\mathbf{x}^0}$ as a function of solution vectors $\underline{\mathbf{x}}$ of previous frequencies is presented.

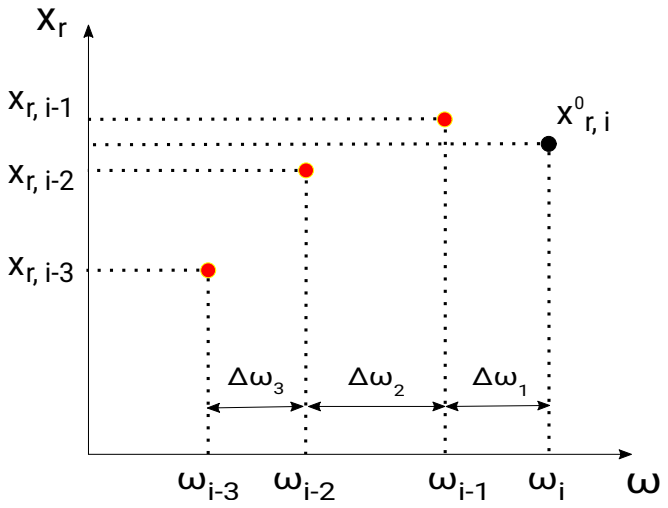

Figure 3.7: Initial estimation of the solution vector at a new frequency

At the beginning of the calculations of the i^{th} frequency, it is necessary to define the number of values used for the initial estimation of solution vector $\underline{\mathbf{x}}$, $\underline{\mathbf{x}_\mathbf{i}^0}$. Supposing that the 3 previous values, $\underline{\mathbf{x_{i-1}}}$, $\underline{\mathbf{x_{i-2}}}$ and $\underline{\mathbf{x_{i-3}}}$, are selected (see Fig. 3.7), the requested expression is the following:

$$\underline{\mathbf{x}_\mathbf{i}^0} = c_1\underline{\mathbf{x_{i-1}}} + c_2\underline{\mathbf{x_{i-2}}} + c_3\underline{\mathbf{x_{i-3}}} \tag{3.9}$$

The constant values c_1, c_2 and c_3 need to be defined. The next step is the expansion of the selected values $\underline{\mathbf{x_{i-1}}}$, $\underline{\mathbf{x_{i-2}}}$ and $\underline{\mathbf{x_{i-3}}}$ using Taylor series. The number of Taylor terms has to be equal to the number of the values.

$$\begin{aligned}
\underline{\mathbf{x_{i-1}}} &= \underline{\mathbf{x_i^0}} - \Delta\omega_1 \left(\frac{\partial \underline{\mathbf{x}}}{\partial \omega}\right)_i + \frac{\Delta\omega_1^2}{2}\left(\frac{\partial^2 \underline{\mathbf{x}}}{\partial \omega^2}\right)_i + O(\Delta\omega^3) \\
\underline{\mathbf{x_{i-2}}} &= \underline{\mathbf{x_i^0}} - (\Delta\omega_1 + \Delta\omega_2) \left(\frac{\partial \underline{\mathbf{x}}}{\partial \omega}\right)_i + \frac{(\Delta\omega_1 + \Delta\omega_2)^2}{2}\left(\frac{\partial^2 \underline{\mathbf{x}}}{\partial \omega^2}\right)_i + O(\Delta\omega^3) \\
\underline{\mathbf{x_{i-3}}} &= \underline{\mathbf{x_i^0}} - (\Delta\omega_1 + \Delta\omega_2 + \Delta\omega_3 \left(\frac{\partial \underline{\mathbf{x}}}{\partial \omega}\right)_i + \frac{(\Delta\omega_1 + \Delta\omega_2 + \Delta\omega_3)^2}{2}\left(\frac{\partial^2 \underline{\mathbf{x}}}{\partial \omega^2}\right)_i + O(\Delta\omega^3)\ ,
\end{aligned} \tag{3.10}$$

where $O(\Delta\omega^3)$ are higher-order terms that are ignored.

Substituting Eq. 3.10 in Eq. 3.9 leads to:

$$\begin{aligned}
\underline{\mathbf{x_i^0}} = (c_1 + c_2 + c_3)\underline{\mathbf{x_i^0}} + [-c_1 \cdot \Delta\omega_1 - c_2 \cdot (\Delta\omega_1 + \Delta\omega_2) - c_3 \cdot (\Delta\omega_1 + \Delta\omega_2 + \Delta\omega_3)] \left(\frac{\partial \underline{\mathbf{x}}}{\partial \omega}\right)_i + \\
\frac{1}{2}[c_1 \cdot \Delta\omega_1^2 + c_2 \cdot (\Delta\omega_1 + \Delta\omega_2)^2 + c_3 \cdot (\Delta\omega_1 + \Delta\omega_2 + \Delta\omega_3)^2 \left(\frac{\partial^2 \underline{\mathbf{x}}}{\partial \omega^2}\right)_i + O(\Delta\omega^3)
\end{aligned} \tag{3.11}$$

The two sides of Eq. 3.11 are equal to each other, if the following equations apply:

$$\begin{aligned}
c_1 + c_2 + c_3 &= 1 \\
c_1 \cdot \Delta\omega_1 + c_2 \cdot (\Delta\omega_1 + \Delta\omega_2) + c_3 \cdot (\Delta\omega_1 + \Delta\omega_2 + \Delta\omega_3) &= 0 \\
c_1 \cdot \Delta\omega_1^2 + c_2 \cdot (\Delta\omega_1 + \Delta\omega_2)^2 + c_3 \cdot (\Delta\omega_1 + \Delta\omega_2 + \Delta\omega_3)^2 &= 0
\end{aligned} \tag{3.12}$$

Eq. 3.12 can also be expressed in matrix form:

$$\begin{bmatrix} 1 & 1 & 1 \\ \Delta\omega_1 & \Delta\omega_1 + \Delta\omega_2 & \Delta\omega_1 + \Delta\omega_2 + \Delta\omega_3 \\ \Delta\omega_1^2 & (\Delta\omega_1 + \Delta\omega_2)^2 & (\Delta\omega_1 + \Delta\omega_2 + \Delta\omega_3)^2 \end{bmatrix} \cdot \begin{bmatrix} c_1 \\ c_2 \\ c_3 \end{bmatrix} = \begin{bmatrix} 1 \\ 0 \\ 0 \end{bmatrix} \tag{3.13}$$

The selection of K previous values leads to Eq. 3.14, which is the general form of Eq. 3.13:

$$\begin{bmatrix} 1 & 1 & \cdots & 1 \\ \sum_{i=1}^{1}\Delta\omega_i & \sum_{i=1}^{2}\Delta\omega_i & \cdots & \sum_{i=1}^{K}\Delta\omega_i \\ (\sum_{i=1}^{1}\Delta\omega_i)^2 & (\sum_{i=1}^{2}\Delta\omega_i)^2 & \cdots & (\sum_{i=1}^{K}\Delta\omega_i)^2 \\ \vdots & \ddots & \ddots & \vdots \\ (\sum_{i=1}^{1}\Delta\omega_i)^{K-1} & (\sum_{i=1}^{2}\Delta\omega_i)^{K-1} & \cdots & (\sum_{i=1}^{K}\Delta\omega_i)^{K-1} \end{bmatrix} \cdot \begin{bmatrix} c_1 \\ c_2 \\ c_3 \\ \vdots \\ c_K \end{bmatrix} = \begin{bmatrix} 1 \\ 0 \\ 0 \\ \vdots \\ 0 \end{bmatrix}, \tag{3.14}$$

If the frequency step is constant and equal to $\Delta\omega$, Eq. 3.14 is simplified to:

$$\begin{bmatrix} 1 & 1 & \cdots & 1 \\ \Delta\omega & 2\Delta\omega & \cdots & K\cdot\Delta\omega \\ \Delta\omega^2 & (2\Delta\omega)^2 & \cdots & (K\cdot\Delta\omega)^2 \\ \vdots & \ddots & \ddots & \vdots \\ \Delta\omega^{K-1} & (2\Delta\omega)^{K-1} & \cdots & (K\cdot\Delta\omega)^{K-1} \end{bmatrix} \cdot \begin{bmatrix} c_1 \\ c_2 \\ c_3 \\ \vdots \\ c_K \end{bmatrix} = \begin{bmatrix} 1 \\ 0 \\ 0 \\ \vdots \\ 0 \end{bmatrix} \tag{3.15}$$

For the case of 3 equidistant values, the unknown coefficients c_1, c_2 and c_3 are given by:

$$\begin{bmatrix} 1 & 1 & 1 \\ \Delta\omega & 2\Delta\omega & 3\Delta\omega \\ \Delta\omega^2 & (2\Delta\omega)^2 & (3\Delta\omega)^2 \end{bmatrix} \cdot \begin{bmatrix} c_1 \\ c_2 \\ c_3 \end{bmatrix} = \begin{bmatrix} 1 \\ 0 \\ 0 \end{bmatrix} \rightarrow \begin{bmatrix} c_1 \\ c_2 \\ c_3 \end{bmatrix} = \begin{bmatrix} 3 \\ -3 \\ 1 \end{bmatrix} \tag{3.16}$$

Hence, the expression for the estimation $\underline{\mathbf{x}_\mathbf{i}^\mathbf{0}}$ is the following:

$$\underline{\mathbf{x}_\mathbf{i}^\mathbf{0}} = 3\underline{\mathbf{x}_\mathbf{i-1}} - 3\underline{\mathbf{x}_\mathbf{i-2}} + \underline{\mathbf{x}_\mathbf{i-3}} \tag{3.17}$$

For the simulations of the current thesis, initialization is based on the previous 1, 2 or 3 values. The expressions for these cases are presented in Table 3.2.

It is clear that this method is used only if the previous values are available. Therefore, for the initialization of the calculations at the first frequency, a random vector of low values $\underline{\mathbf{x}_\mathbf{00}}$ is used (values of 1-2%c_r for all the elements of the vector). For the same reason, the calculations of the second frequency are initialized from the solution vector of the previous frequency $\underline{\mathbf{x}_\mathbf{i-1}}$. If the previous step did not converge, the vector $\underline{\mathbf{x}_\mathbf{00}}$ is necessarily used.

Table 3.2: Expressions for the initial estimation of solution vector

Number of values	Expression
1	$\underline{\mathbf{x_i^0}} = \underline{\mathbf{x_{i-1}}}$
2	$\underline{\mathbf{x_i^0}} = 2\underline{\mathbf{x_{i-1}}} - \underline{\mathbf{x_{i-2}}}$
3	$\underline{\mathbf{x_i^0}} = 3\underline{\mathbf{x_{i-1}}} - 3\underline{\mathbf{x_{i-2}}} + \underline{\mathbf{x_{i-3}}}$

3.3.4 Evaluation of Transient Response

Results of transient analysis are used as a reference for the results of the method presented in the thesis.

The library *SciPy.integrate* of *Python* contains numerous explicit and implicit methods to solve initial value problems of ordinary differential equations. Explicit methods calculate the state at a later time $x(t + \Delta t)$ using the state at the current time $x(t)$ as followed:

$$x(t + \Delta t) = F(x(t)) \tag{3.18}$$

On the other hand, implicit methods solve equations that involve both the current and the later state to calculate $x(t + \Delta t)$:

$$G(x(t), x(t + \Delta t)) = 0 \tag{3.19}$$

The choice between explicit and implicit methods is based on the stiffness of the system. Stiff systems cannot be solved using explicit methods because they require extremely small time steps Δt so that they do not present numerical instabilities. For this reason, stiff systems are usually solved with implicit methods that require remarkably less computational time.

SciPy.integrate contains explicit (e.g. third and fifth-order) and implicit (fifth-order) Runge-Kutta methods and others based on backward differentiation formulas.

Hence, for the purposes of the present thesis, the system of Eq. 2.9 is solved in the time domain using the method *RK45* from the routine *solve_ivp* of *SciPy.integrate*. The error is controlled assuming accuracy of the fourth-order method, but steps are taken using the fifth-order accurate formula (local extrapolation is done) [32].

The most important parameters, set for the implementation of the method in *Python*, are the following: The time span *t_span* defines the interval of integration for the solver. The initial condition *y0* gives the initial state of the solution vector.

3.4 Comparison of The Multi-Harmonic Method to Transient Analysis

The algorithm of the linearization method is presented in Section 3.2 (also schematically in Fig 3.6). It is reminded that the study concerns a Jeffcott rotor supported by two squeeze film dampers in parallel with squirrel cages. The validity of the method is examined by comparing its results to transient response.

The following five parameters are selected in order to investigate the accuracy of the method in a variety of cases:

- G quality grades 2.5, 6.3 and 16 (according to [1])
- Slenderness ratio (length to diameter ratio) of the shaft L_s/D_s from 5 to 10
- Squirrel cage stiffness in x direction to shaft stiffness ratio $k_{c,x}/k_s$ from 0.2 to 1
- Squirrel cage stiffness in y direction to shaft stiffness ratio $k_{c,y}/k_s$ from 0.2 to 1
- The weight of the disk and the journals is considered or not.

Neglecting the total weight of the rotor-bearing system leads to the whirling of the journals about the centerline in either circular or elliptic orbits. On the other hand, if the weight is taken into account, the squirrel cage stiffness plays a crucial role to the position of the orbit center in y direction.

Circular and elliptic journal orbits about the centerline are presented in Fig. 3.8 and 3.9.

A wide variety of cases are examined. The circular shape of the orbits in Fig. 3.8 are due to the symmetry of the model in x and y direction. This leads to identical responses in x and y direction. The consideration of the weight leads to asymmetry in the two directions and usually to elliptic orbits.

In the cases of Fig. 3.8, orbits of small (25%c_r) and large (about 75%c_r) radii are examined, for low and high balance grades G, respectively. Furthermore, various types of curve shapes are observed: In the first case, the resonance bears resemblance to linear resonances. On the contrary, the jump phenomenon of the third case is a typical characteristic of nonlinear dynamics.

As expected from the preceding analysis of Chapter 2, the first-order harmonic is sufficient for the perfect approximation of the circular orbits about the bearing center, even close to the resonance. The small difference observed in the last case of Fig. 3.8 is caused by transient phenomena. The difference would not be present, if the acceleration of the transient simulation tended to zero (steady-state analysis).

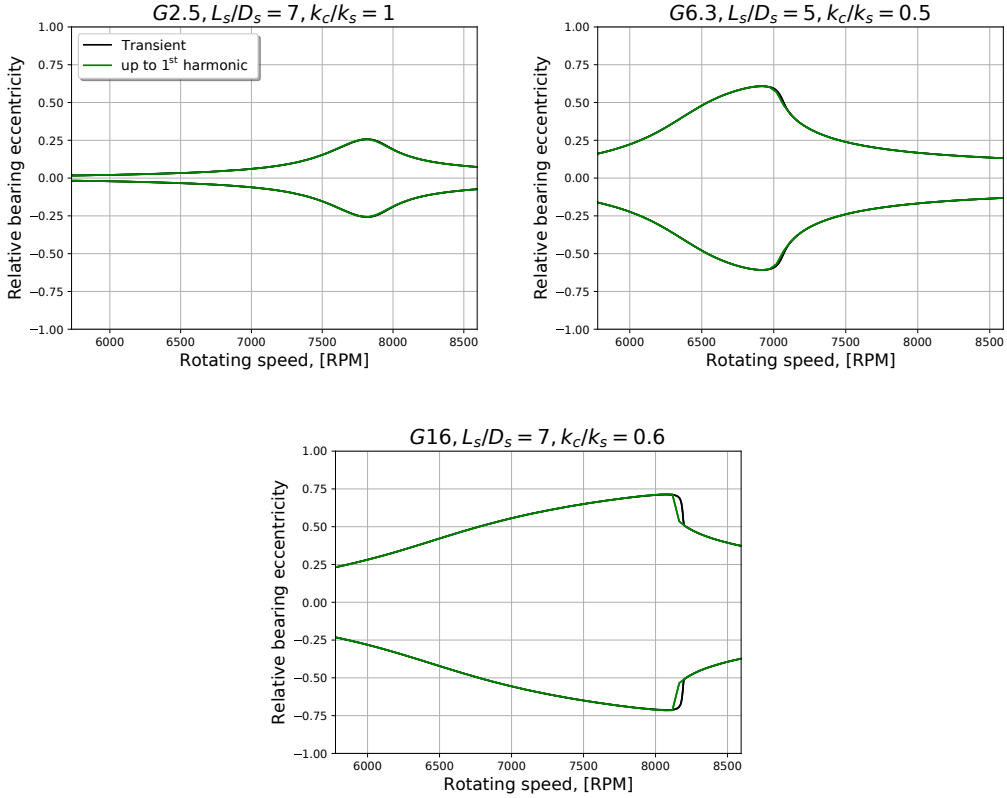

Figure 3.8: Comparison to transient results for circular orbits about the centerline

The orbits of Fig. 3.9 differ from those of Fig. 3.8 because of dissimilar squirrel cage stiffness in x and y direction. For this reason, the critical speed ω_{cr} in y direction is lower (ω_{cr} is proportional to the square root of stiffness).

It is clear that the first response of Fig. 3.9 is approximated exceptionally using only the first order and the third-order harmonic is not needed. However, this is not true for the response of the second case in x direction, where the third order offers a significant improvement of about 10%. Finally, in the third case, the response in x and y direction are similar to each other because of the small difference in squirrel cage stiffness in the two directions. It is reminded that even-order harmonics always equals to 0 for orbits about the centerline.

Finally, in Fig. 3.10, the weight of the rotor-bearing system is taken into account. As a result, the orbit center is displaced to $(0, y_{0,w})$. It is reminded that y_0 (total displacement in y direction) is also a function of the rotational speed, as the mean value of SFD forces varies in the speed range. Therefore:

$$y_0(\Omega) = y_{0,SFD}(\Omega) + y_{0,w} \ , \tag{3.20}$$

where $y_{0,SFD}$ is the contribution of the mean value of SFD force and $y_{0,w}$ is the displacement due to weight.

In order to examine the validity of the multi-harmonic method for off-centered orbits too, the response in y direction is presented in Fig. 3.10, for three cases of different

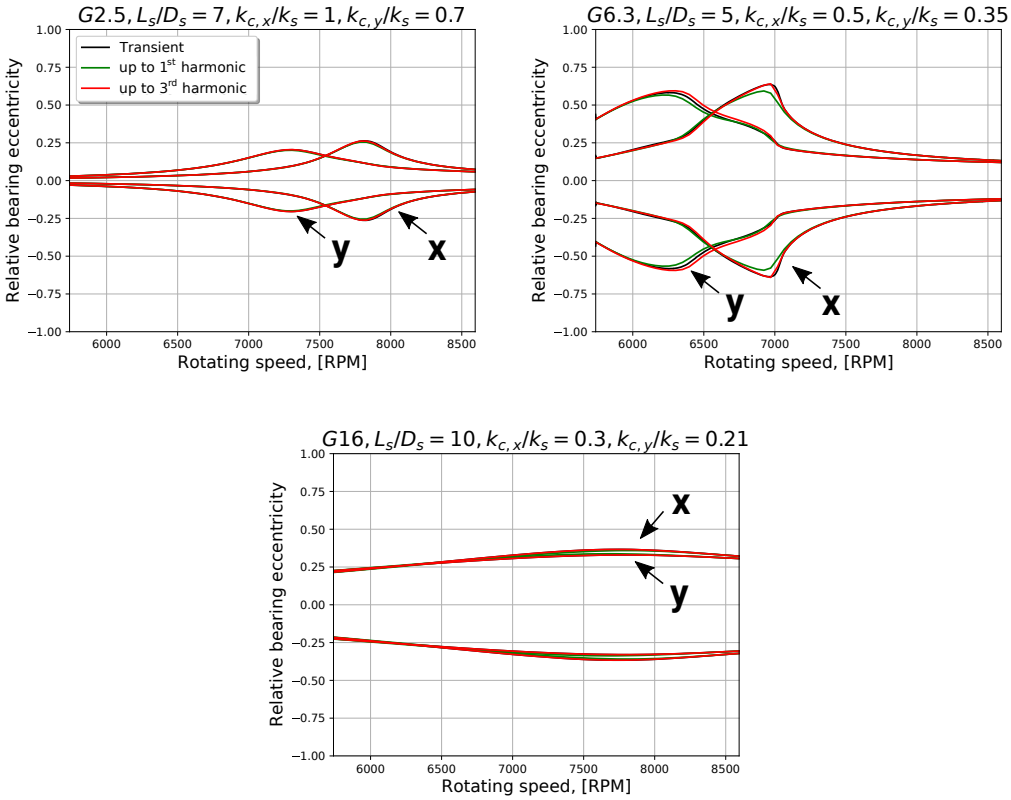

Figure 3.9: Comparison to transient results for elliptic orbits about the centerline

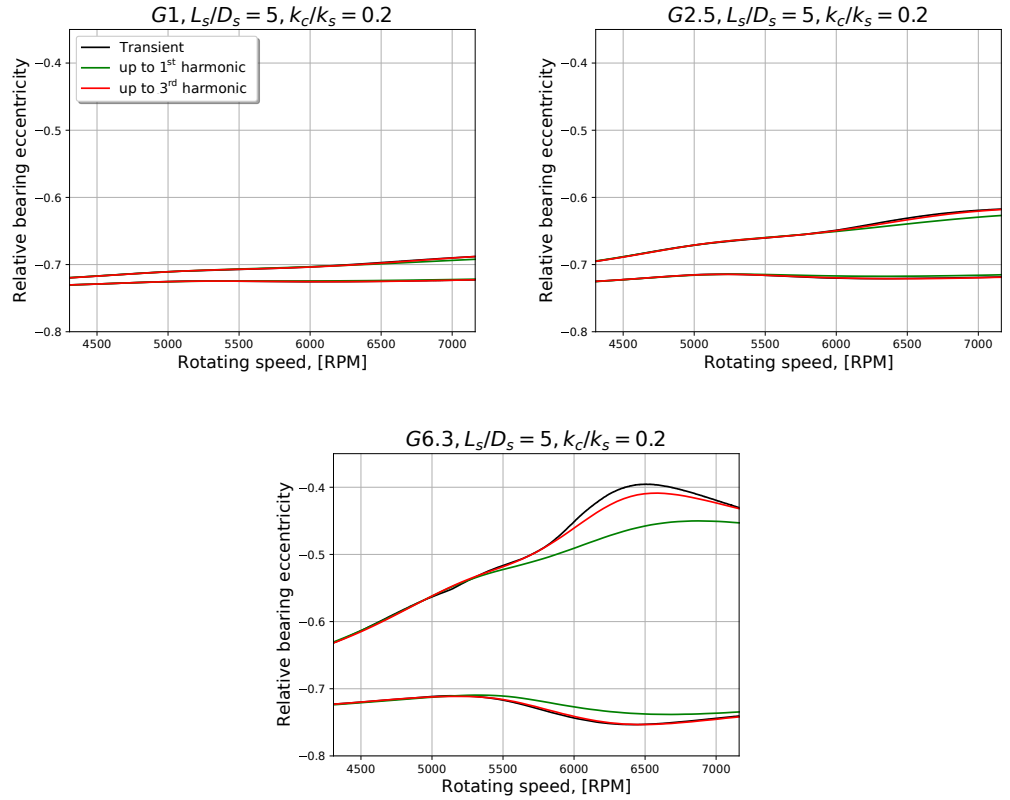

Figure 3.10: Comparison to transient results for orbits about an off-centered point

balance quality grades (G1, G2.5, G6.3). The influence of weight is clear, as the journal whirls between $-0.75c_r$ and $-0.4c_r$ in y direction.

In all three cases of Fig. 3.10, the displacement due to weight $y_{0,w}$ equals to $-0.74c_r$ and the journal perturbates close to the stationary outer ring. As a result, SFD force in y direction and $y_{0,SFD}$ have large positive values. In fact, $y_{0,SFD}$ grows larger, as rotational speed increases. Altogether, the journal whirls about $y_0 > y_{0,w}$.

The importance of higher-order harmonics for the approximation of journal responses is emphasized once more, especially for orbits of large radii and/or large static eccentricity.

3.5 Comparison of The Multi-Harmonic Method to *MSC Nastran* Nonlinear Harmonic Balance

The multi-harmonic method is also validated by comparing its results to *MSC Nastran* nonlinear harmonic balance. A case of centered circular orbits is examined. The response is presented in Fig. 3.11.

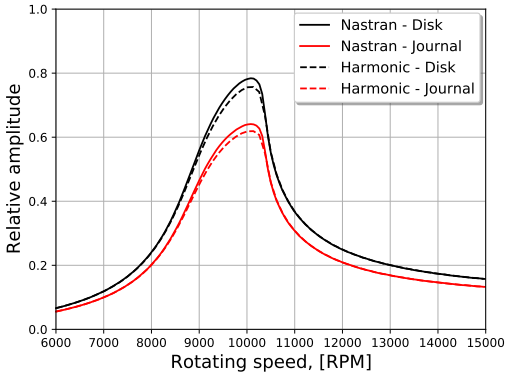

Figure 3.11: Comparison to *MSC Nastran* nonlinear harmonic balance

As explained above, only the first-order harmonic is required for the specific case. The two methods provide similar results, since the relative error is about 3% for both the disk and the journal response. However, this small error may be due to a difference on the application of the short bearing approximation. In any case, the approximation of *MSC Nastran* nonlinear harmonic balance to such extent is a very important result for the multi-harmonic method.

4 Rotor Dynamic Simulations of Realistic Aircraft Engines

4.1 Modeling Details

In the current Section, the modeling procedure followed for different jet engines components is explained. MTU in-house tools are used for the purposes of modeling.

First of all, rotor(s) and casing are modeled as a series of elements of real dimensions. Their physical properties (mass and moments of inertia) are derived from their geometry and material properties. The properties of materials can also be a function of temperature. Each element might also have point masses and/or moments of inertia attached to it. The shape can either be cylindrical or conical depending on the position of the element in the engine. When radius changes along the axial direction of the engine, cylindrical elements are used. The number of DOFs for each node can be up to 6.

A standard jet engine contains large fan blades, compressor and turbine moving and stationary stages of blades. Blade geometry is very complex to be modeled in detail for rotordynamics simulations, thus they are usually modeled as rigid bodies with inertial characteristics (mass and moment of inertia). These elements are placed in the position of the blade's center of gravity.

Bearings and squeeze film dampers are usually modeled as a spring parallel to a damper and, rarely, an extra mass. These three elements provide stiffness, damping and inertia, respectively. The bearings can be constant, speed dependent or, even, nonlinear.

Bolts are used to connect two or more machine elements rigidly. Thus, they are modeled as rigid springs. An additional mass and moment of inertia can be added at their position in the engine. Flanges also connect parts of the engine and the connection is maintained by bolts. They are also modeled as springs.

Finally, squirrel cages are centering spring mechanisms that are used in series with squeeze film dampers. In general, they are linear springs, hence they are modeled as such.

The information about the modeling provided above is indicative. In general, the accuracy of the models varies considerably depending on the desired accuracy.

The simulations of the current Chapter concern the model of Fig. 4.1. The jet engine consists of 2 counter-rotating rotors, Low Pressure (LP) rotor (in blue, yellow and magenta) and High Pressure (HP) rotr (in green), and the casing (in red). The speed ratio

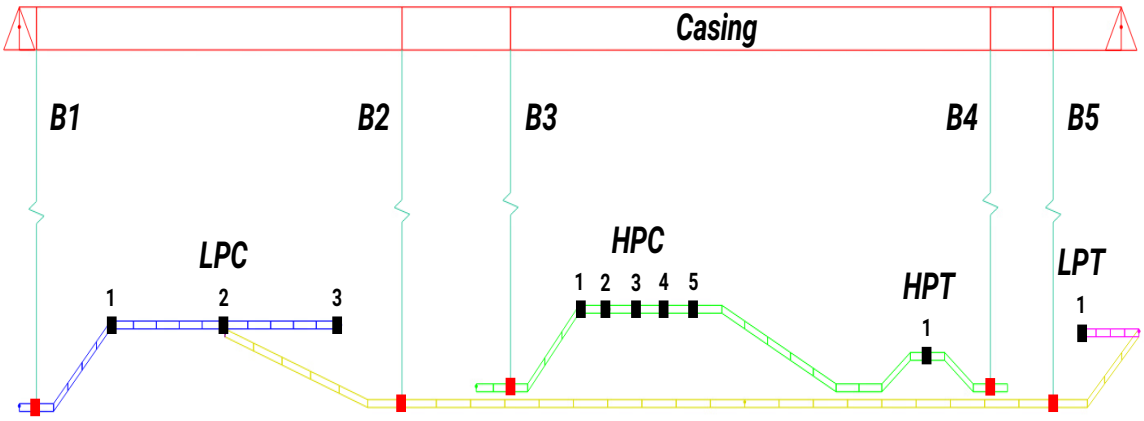

Figure 4.1: Realistic engine model

Ω_{HP}/Ω_{LP} equals to -1.6. There are three Low Pressure Compressor (LPC) stages and five High Pressure Compressor (HPC) stages, as well as one High Pressure Turbine (HPT) and one Low Pressure Turbine (LPT) stages. Their place is symbolized by black squares. The 5 bearings (B1-B5) are depicted as light blue springs. The nodes where the bearings are connected to the rotor are symbolized by red squares. Finally, the grey dashed line is the centerline of the engine. Because of the symmetry about the centerline, only half the engine is depicted in Fig. 4.1.

4.2 Linear Dynamic Model: Constant and Speed Dependent Bearing Coefficients

For linear calculations, MTU in-house tools are used. The matrices of the system can either be constant or speed dependent. Speed dependent stiffness and damping coefficients are usually introduced to the system by bearings and squeeze film dampers. The most characteristic example is the stiffness of rolling element bearings, which varies significantly with rotatonal speed.

The two rotors counter-rotate with a speed ratio $\Omega_{HP}/\Omega_{LP} = -1.6$. Therefore, the speed ranges of HP and LP rotor are 0-30000 RPM and 0-18750 RPM, respectively. The casing is connected stiffly to the ground, thus its motion is limited. As a result, the two rotors revolve and whirl independently since they are only connected to each other through the casing.

The FW critical speeds of the rotors are calculated through modal analysis. HP rotor has two critical speeds at 11501 and at 20519 RPM. On the other hand, LP rotor has three critical speeds at 9323, 11791 and 18700 RPM. The corresponding modes are displayed in Fig. 4.2 and 4.3. Moreover, the distribution of the system's potential energy between the rotors and the bearings are presented in Tables 4.1 and 4.2.

The first HP mode is cylindrical and the second one is conical. The potential energy of the rotor is relatively low for both modes.

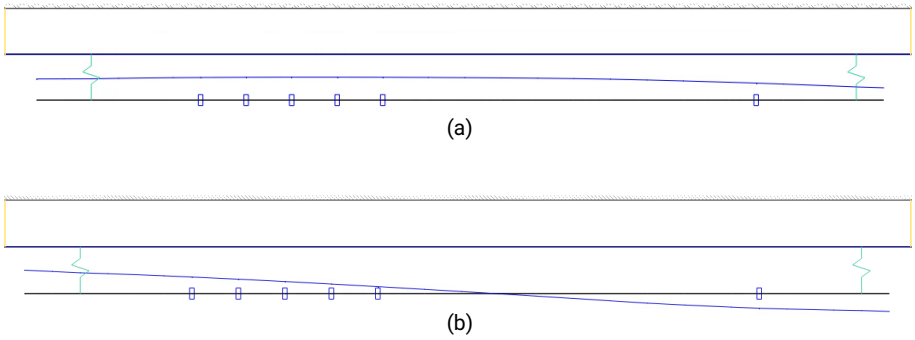

Figure 4.2: HP rotor modes. a) at 11501 RPM. b) at 20519 RPM

Table 4.1: Distribution of HP system potential energy at critical speeds

Critical speed [RPM]	HP rotor	Bearing B3	Bearing B4
11501	15.6%	49.3%	35.1%
20519	16.8%	36.8%	46.4%

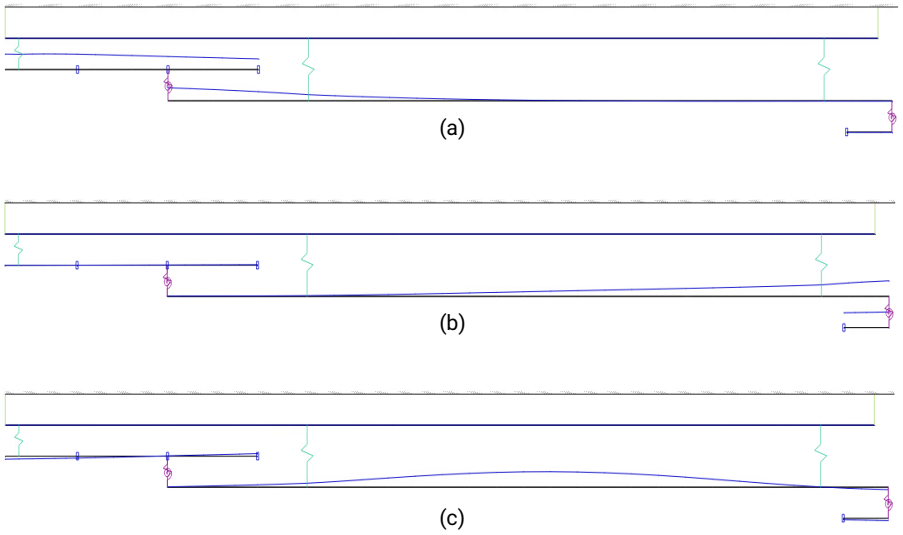

Figure 4.3: LP rotor modes. a) at 9323 RPM. b) at 11791 RPM. c) at 18700 RPM

Table 4.2: Distribution of LP system potential energy at critical speeds

Critical speed [RPM]	LP rotor	Bearing B1	Bearing B2	Bearing B5
9323	18.1%	58.4%	23.4%	0.1%
11791	17.1%	0%	0.3%	82.6%
18700	74.6%	4.2%	21.1%	0.1%

On the other hand, the fist two LP modes are bounce modes and the third one is a bending mode. The potential energy of the rotor is fairly high (74.6%) for the third LP mode.

Subsequently, the unbalance response of the engine is presented in Fig. 4.1. Both static and dynamic unbalance cases are examined for the following nodes:

- 4 nodes of HP rotor
  - 2 bearing nodes (3, 24)
  - 1 HPC stage node (7)
  - 1 HPT stage node (21)
- 5 nodes of LP rotor
  - 3 bearing nodes (2, 24, 43)
  - 1 LPC stage node (7)
  - 1 LPT stage node (48)

The speed dependent stiffness and damping coefficients vary from 50% to 150% of the constant coefficients. The lowest and highest values correspond to the minimum and maximum speed of each rotor, respectively. Speed dependent coefficients are considered to be proportional to rotational speed, therefore linear interpolation is used for intermediate speeds. It is reminded that the rotors counter-rotate with different speeds.

The results for both rotors are presented in Fig. 4.4 and 4.5.

The influence of speed dependent coefficients on critical speeds and amplitude values is clear. If $\omega_{cr} < 0.5\omega_{max}$, the critical speeds get smaller (because of lower stiffness) and the amplitudes get larger (because of lower damping). On the other hand, if $\omega_{cr} > 0.5\omega_{max}$, the amplitudes get smaller and the critical speeds move to higher values.

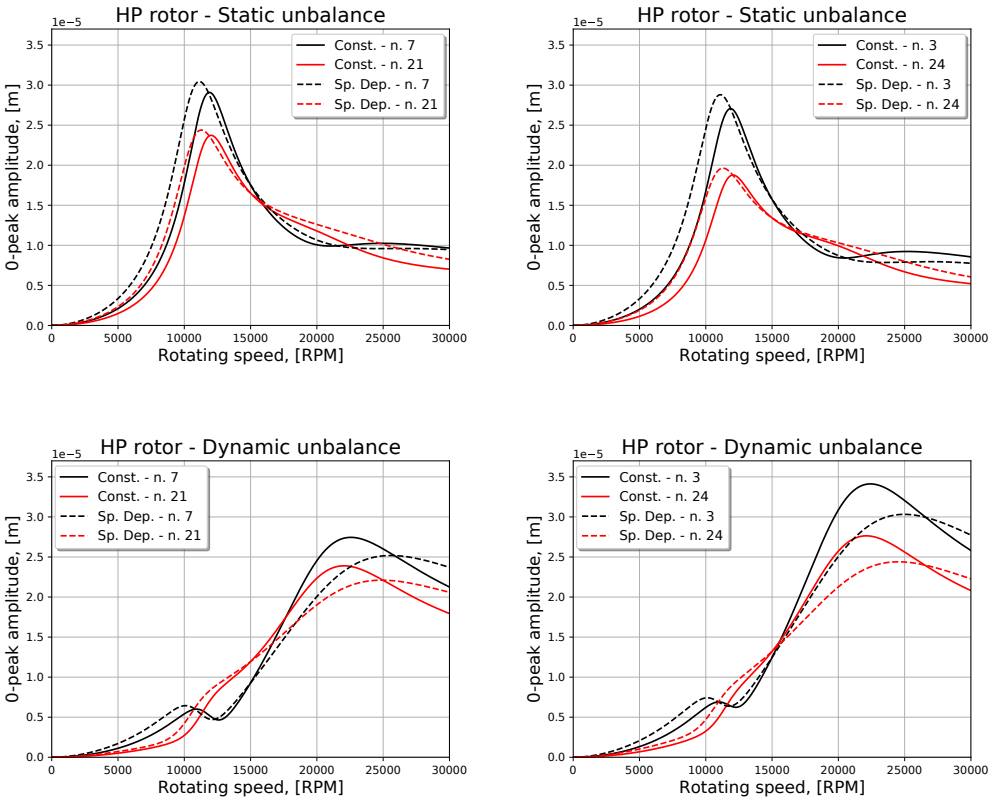

Figure 4.4: HP rotor unbalance response with constant and speed dependent bearing coefficients

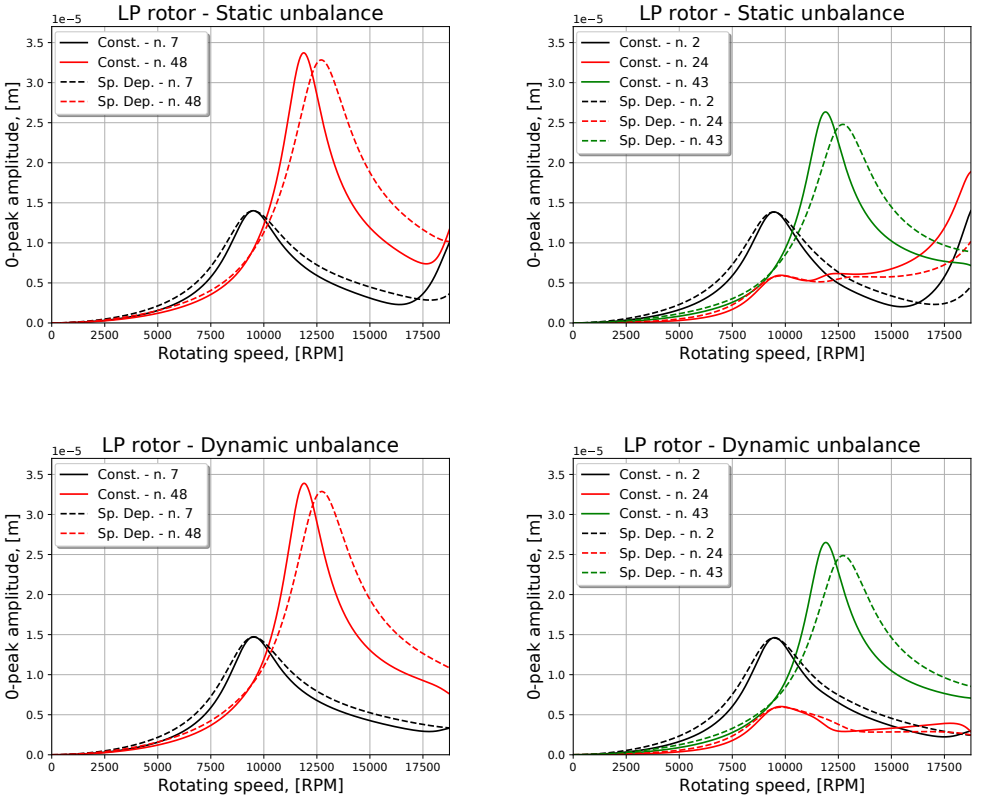

Figure 4.5: LP rotor unbalance response with constant and speed dependent bearing coefficients

4.3 Unbalance Response Using The Multi-Harmonic Method

Henceforward, it is preferred to only present results of the multi-harmonic method that concern the HP rotor, since LP rotor has over 200 DoFs and the simulations are extremely time-consuming, especially when multiple harmonics are considered. The nonlinear multi-harmonic method is applied to HP rotor for a variety of cases. The parameters of the following simulations are:

- The unbalance case (static or dynamic)
- The weight of the HP rotor
- The stiffness of B3 squirrel cage
- The number of SFDs
- The number of harmonics

4.3.1 Unbalance Response with SFD at The Position B3 and Balance Grade G25

Jet engines are extremely light in order to improve aircraft performance, especially in military applications. Moreover, both squirrel cages B3 and B4 are highly stiff. Therefore, the center of the journal orbit does not move significantly from the centerline of the engine. The maximum deflection is 7.7% of the radial clearance and the deflection of the B3 and B4 journals is 6.9% and 4.8%, respectively. The system is also symmetric and the response in x and y direction are identical to each other. As a result, the second-order harmonic, as well as higher-order harmonics, are insignificant. At first, only the first-order harmonic is used to compare the results of the method to those of linear harmonic analysis with constant coefficients.

The first group of results concerns both static and dynamic unbalance response. Each unbalance has magnitude of 500 g·mm and the phase difference between them equals to 0^o (static) or 180^o (dynamic). The unbalance used corresponds to balance grade G25, which is a higher value than those used in Chapter 3.

A squirrel cage and a nonlinear squeeze film damper are employed at the position B3, while a squirrel cage and a bearing of constant damping are used at the position B4. B3 and B4 squirrel cages have stiffness of $8 \cdot 10^7$ N/m and $1.5 \cdot 10^8$ N/m, respectively.

The results of the multi-harmonic method, using just the first-order harmonic in that case, are compared to the linear harmonic response (constant bearing damping coefficients for both bearings). The results are presented in Fig. 4.6 and 4.7.

The constant bearing damping is higher than required, therefore the results of the linear analysis seriously underestimate the amplitudes. In particular, the values calculated

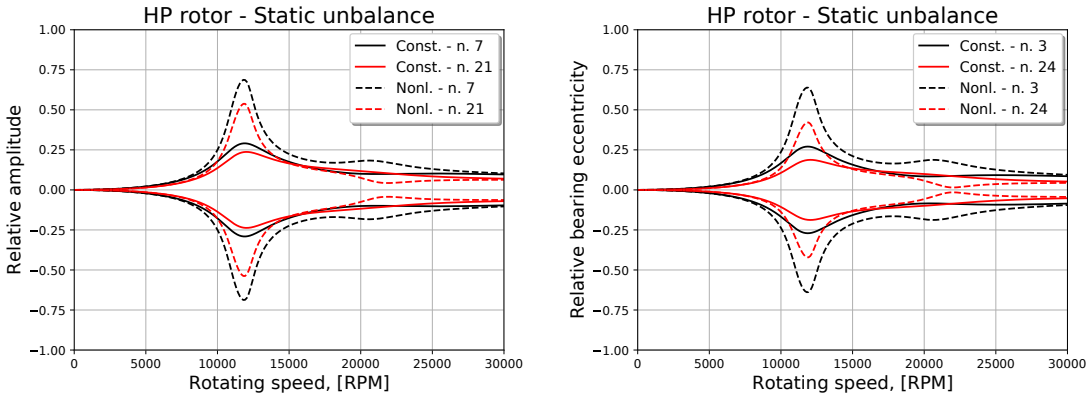

Figure 4.6: HP rotor static unbalance response with constant and nonlinear bearings (SFD employed at B3)

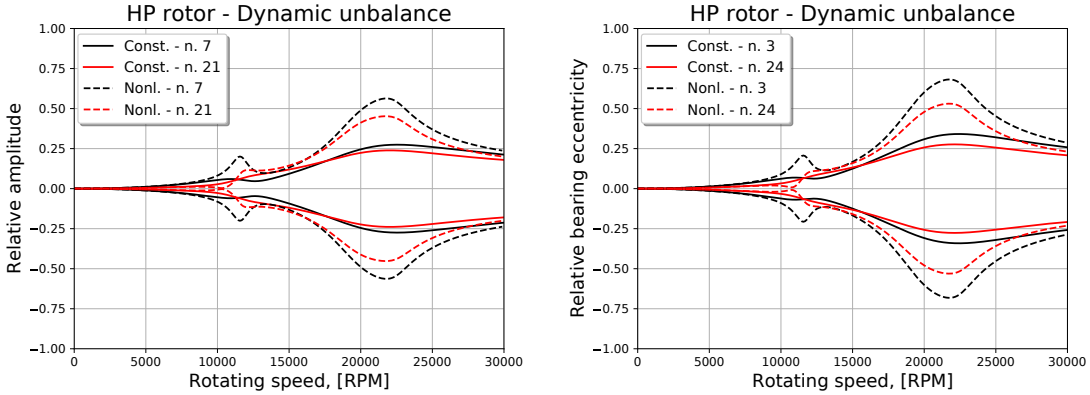

Figure 4.7: HP rotor dynamic unbalance response with constant and nonlinear bearings (SFD employed at B3)

are up to 3 times lower than the nonlinear results. However, the critical speeds are sufficiently approximated by linear analysis. In this case, the influence of stiff squirrel cages on the critical speeds is determinant. In order to observe an important shift of critical speeds, more flexible squirrel cages are required.

4.3.2 Unbalance Response with SFDs at The Positions B3 and B4 and Balance Grade G25

The same unbalance cases are examined for the second group of results. A combination of squirrel cages and nonlinear squeeze film dampers are employed at the positions B3 and B4. B3 and B4 squirrel cages have stiffness of $8 \cdot 10^7$ N/m and $1.5 \cdot 10^8$ N/m, respectively. Once again, only the first-order harmonic is used. The corresponding results are presented in Fig. 4.8 and 4.9.

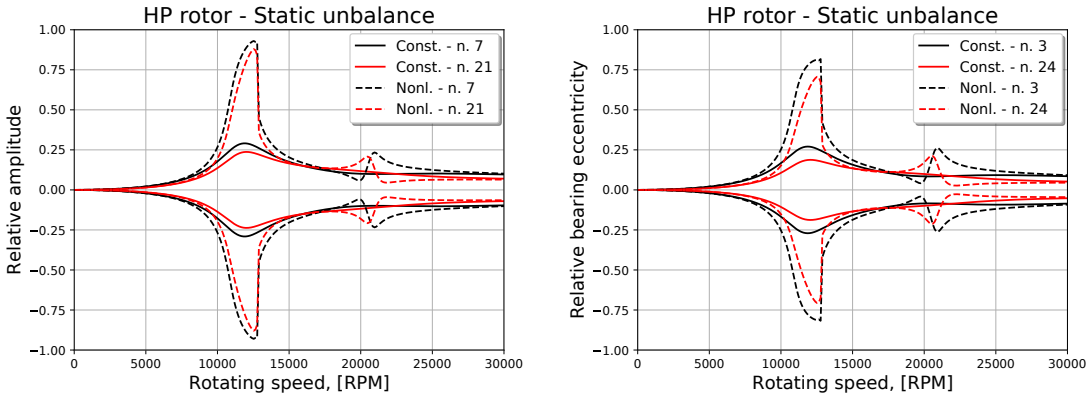

Figure 4.8: HP rotor static unbalance response with constant and nonlinear bearings (SFDs employed at B3 and B4)

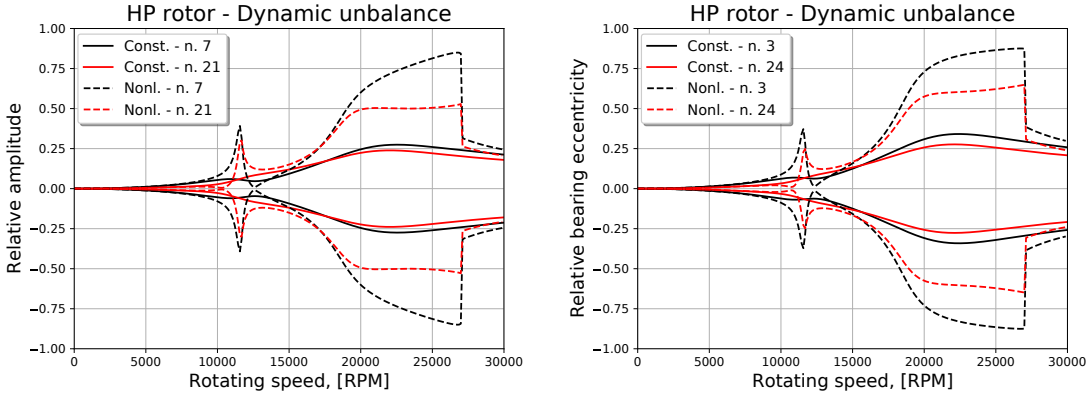

Figure 4.9: HP rotor dynamic unbalance response with constant and nonlinear bearings (SFDs employed at B3 and B4)

Vast difference is observed between the results of the two methods. The use of two SFDs alters the magnitude and the shape of the amplitudes and shifts the critical speeds, especially for the case of dynamic unbalance. The journals whirl at eccentricities close to the radial clearance ($> 90\% c_r$) and jump phenomena are observed.

The results of the multi-harmonic method are validated by comparing its results to *MSC Nastran* nonlinear harmonic balance in Fig. 4.10 and 4.11 for both static and dynamic unbalance. The response of the HPC and HPT stage nodes, as well as the bearing nodes, is presented.

The orbits of the present Subsection are centered and circular, thus only the first-order harmonic is required. The difference between the results of the two methods is minimal and, even, this small difference may be due to a different approach in the implementation of the short bearing approximation.

Moreover, it is highlighted that the calculations of *MSC Nastran* nonlinear harmonic balance are terminated exactly before the jump and, therefore, the entire response is not displayed. On the contrary, the multi-harmonic method succeeds in passing through the jump. All in all, the validation of the results concerning the response of the realistic engine model is crucial for the reliability of the multi-harmonic method.

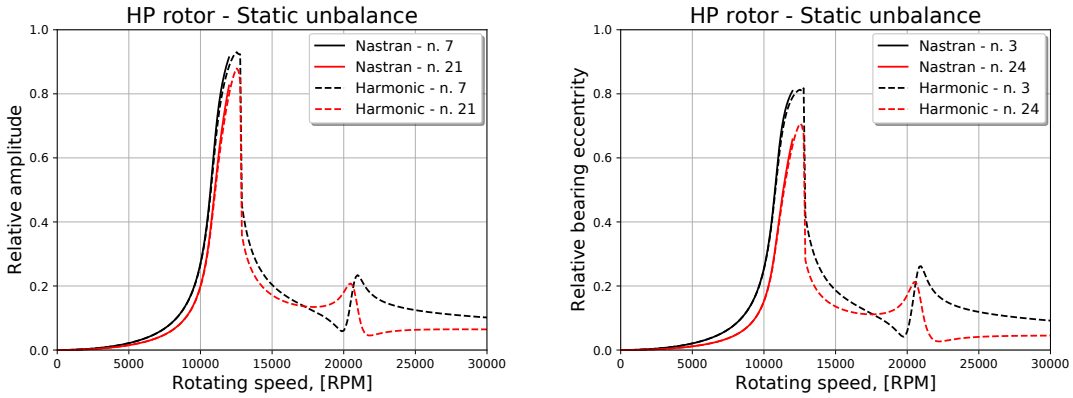

Figure 4.10: Comparison to *MSC Nastran* nonlinear harmonic balance for static unbalance case

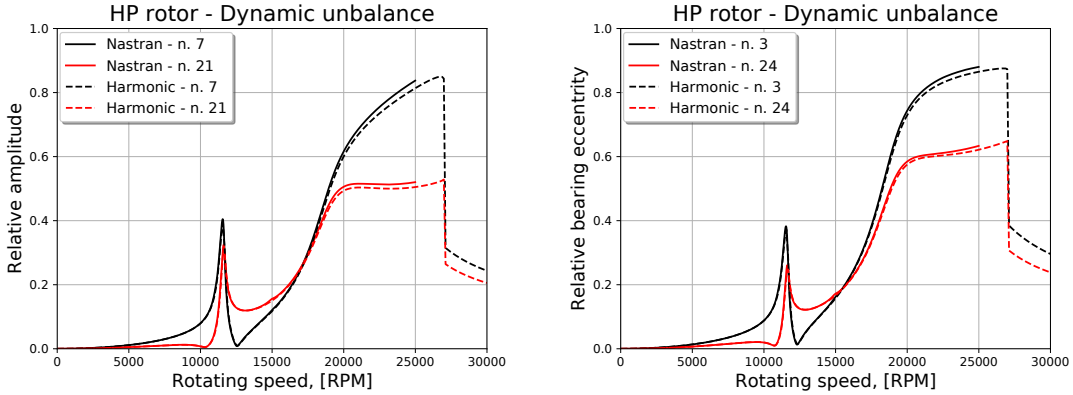

Figure 4.11: Comparison to *MSC Nastran* nonlinear harmonic balance for dynamic unbalance case

4.3.3 Unbalance Response with SFD and Flexible Squirrel Cage at The Position B3 and Balance Grades G2.5 and G6.3

Subsequently, a flexible squirrel cage of stiffness $3 \cdot 10^7$ N/m and a squeeze film damper are employed at the position B3, while a stiff squirrel cage of stiffness $1.5 \cdot 10^8$ N/m and constant damping are used at the position B4. The weight of the LP rotor is doubled, thus much larger static deflection is observed. The deflection of the B3 and B4 journals is now 30.2% and 8.3% of the radial clearance, respectively. The difference between them is larger, since the squirrel cage at the position B4 is five times stiffer than the one at the position B3. The unbalance response is approximated by the zeroth, the first and the second-order harmonics.

The unbalance response of the HPC and HPT stage nodes is examined. The results for balance grade G2.5 and G6.3 are presented in Fig. 4.12 and 4.13, respectively.

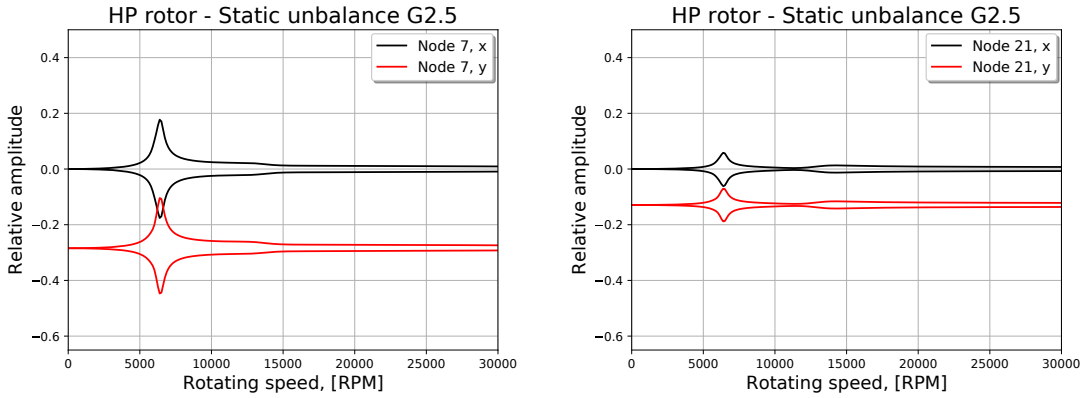

Figure 4.12: HP rotor static unbalance response with nonlinear bearings and balance grade G2.5 (SFD employed at B3)

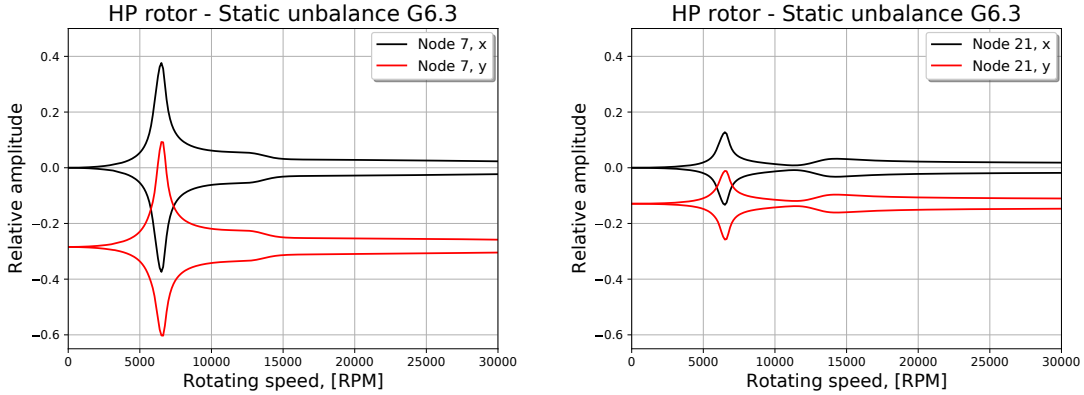

Figure 4.13: HP rotor static unbalance response with nonlinear bearings and balance grade G6.3 (SFD employed at B3)

Only one significant resonance is observed at 6500 RPM for both nodes. The orbits are circular, but their centers are now located at -28.4%c_r for node 7 and -12.9%c_r for node 21. The effect of the second-order harmonic remains minimal at the resonance, since its magnitude is always less than 1% of the radial clearance.

4.3.4 Unbalance Response with SFD and Flexible Non-Symmetric Squirrel Cage at The Position B3 and Balance Grade G6.3

In order to produce elliptic orbits, a squirrel cage with unequal stiffness in x and y direction is employed at the position B3 ($6 \cdot 10^7$ N/m in x and $3 \cdot 10^7$ N/m in y direction). Zeroth, first, second and third-order harmonics are used for the simulation. The results are presented in Fig. 4.14.

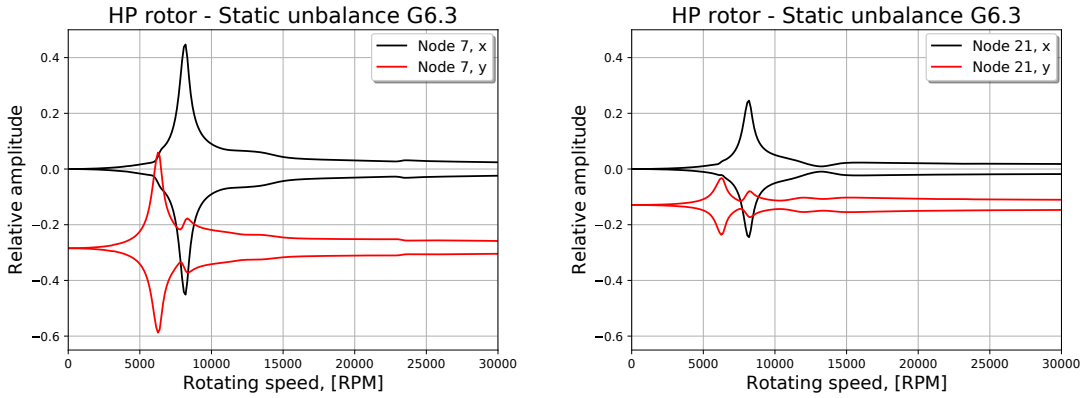

Figure 4.14: HP rotor static unbalance response with nonlinear bearings and balance grade G6.3 (SFD and non-symmetric squirrel cage employed at B3)

The higher squirrel cage stiffness in x direction shifts the critical speed to a higher value (8200 RPM). Moreover, the amplitude in y direction is smaller than the one in x direction for both nodes. The magnitudes of the second and the third-order harmonic remain insignificant (less than 1%c_r).

5 Conclusions and Further Improvement

5.1 Summary and Conclusions

The current thesis examines the effect of speed dependent and nonlinear bearings on the dynamic behaviour of jet engines.

Concerning speed dependent bearings, their influence is important since they move the critical speeds and alter the amplitudes of the system.

The main problem examined in the thesis is the treatment of nonlinear bearings and the manner to include them in dynamic systems in the frequency domain. Hence, a new multi-harmonic method for the linearization of nonlinear bearing and SFD forces is presented. The main idea of the method is the approximation of nonlinear bearing or SFD forces along the orbit. Forces are approximated as sums of N harmonics of the rotational speed using Discrete Fourier Transform. Based on the harmonics, unbalance response is calculated by multi-harmonic analysis. The steps of the method are repeated until convergence is achieved.

In Chapter 2, expressions for nonlinear SFD forces are derived by applying short bearing approximation. These forces are approximated by harmonics in order to be introduced to the multi-harmonic method. Although SFD forces are considered, the method is general and can be used on any type and model of squeeze film damper, linear (speed dependent or constant) or nonlinear bearing.

In Chapters 3 and 4, results of the method for a wide variety of models and parameters are presented. A Jeffcott rotor model of 4 degrees of freedom and a Jeffcott rotor FEM model are considered in Chapter 3, while a realistic aircraft engine model is examined in Chapter 4. The results of the method are compared to those of linear harmonic analysis with constant bearing damping. It is shown that linear methods fail to predict engine's unbalance response and they generally are unreliable. Hence, it is necessary to resort to nonlinear methods, such as the multi-harmonic method. Small and large amplitudes, circular and elliptic, as well as centered and off-centered journal orbits are examined and the results of the multi-harmonic method are presented in detail.

For the majority of cases, the method achieves to approximate perfectly the transient response using only the first or the first three harmonics (along with zeroth order, which originates from the weight and the mean value of the forces). Specifically, the first-order harmonic is sufficient for circular centered orbits and only the odd-order harmonics are required for elliptic centered orbits. Concerning off-centered orbits, there are no general rules concerning the requisite number of harmonics. Nevertheless, the first-order harmonic seems to be sufficient for off-centered circular orbits. With the simulations

of Chapter 3 on the Jeffcott rotor model, it was shown that the second and the third-order harmonic improve the approximation by up to 10% for off-centered elliptic orbits. However, these two harmonics do not change significantly the approximative response in the simulations of Chapter 4 on a realistic HP rotor. All things considered, the zeroth and first-order harmonics always produce an adequate approximation, while second and third-order harmonics are important for large orbits. Extreme cases of static eccentricities and orbit radii close to the radial clearance can be an exception and even higher-order harmonics may be necessary.

All in all, the validity of the multi-harmonic method has been verified by conducting many simulations on a wide variety of models and conditions. It is verified that it provides excellent results, however there is always room for improvement, especially concerning the numerical procedures involved.

5.2 Further Improvement to The Multi-Harmonic Method

Numerical Optimization

The numerical optimization of the software is critical in order to increase its time-efficiency and its stability.

As mentioned in Chapter 3, in some cases, the method fails to converge after a large number of iterations. This problem is usually observed in cases of high eccentricity (larger than $0.9c_r$). Hence, a solution to this problem could be the introduction of under-relaxation to the software in order to increase its stability. In such manner, when the estimated eccentricity gets larger than the radial clearance c_r, a lower eccentricity value ($< c_r$) is considered in order to continue the calculations.

In cases of failure of convergence, a variable step size could be applied. Namely, when the method diverges at frequency f_1, the software will terminate the calculations at f_1 and start over at $f_2 < f_1$, which is closer to the previously converged frequency. In such manner, the initial estimation will be closer to the real value and the method will hopefully converge. If this is not the case, the step could be reduced again.

Furthermore, the software can be notably faster if Jacobian matrix is treated properly. At the present time, the Jacobian matrix is evaluated at each frequency, which may not be necessary, especially for speeds far from amplitudes where the response does not vary significantly. Also, some derivatives included in the Jacobian matrix could be calculated analytically by user-defined formulas.

Another idea would be the examination of other *Python* solvers, except for *fsolve*, in order to decide which is the optimal routine, in terms of stability and time-efficiency, for the numerical solution of the system.

Cooperation with Linear Harmonic Analysis

A few amplitudes are normally observed in the speed range of jet engines and, far from them, unbalance response is minimal. Therefore, a variable frequency step could be applied in order to reduce the number of frequencies evaluated. In such manner, small frequency steps would be used for frequencies close to resonance and large steps for frequencies far from them.

Furthermore, in order to avoid unnecessary time-consuming calculations, linear analysis could be used in combination with the multi-harmonic method. If an approximative calculation of the critical speeds is provided by linear analysis, the multi-harmonic method could be applied only at the frequencies close to resonance. Similarly, the calculation could involve a different number of harmonics depending on the distance of each frequency from the critical speeds.

Finally, the method could be very useful during the preliminary design stages of engines. The nonlinear method using just the first-order harmonic could be applied close to critical speeds. In such manner, a record of the forces exerted by the SFDs to the rotor close to critical speeds can be constructed. Afterwards, when some parameters change, there will not be necessary to conduct again the nonlinear analysis. A linear analysis with the recorded SFD forces can provide adequate approximation and accelerate the design process. Nevertheless, it is highlighted that this method can only work for similar rotors and squeeze film dampers.

References

[1] ISO 1940/1:2003(E). Mechanical vibration - balance quality requirements for rotors in a constant (rigid) state - part 1: Specification and verification of balance tolerances. Standard, International Organization for Standardization.

[2] G. Adiletta and L. Della Pietra. The squeeze film damper over four decades of investigations. part 1: Characteristics and operating features. *Shock and Vibration Digest*, 34(2):3–26, 2002.

[3] G. Adiletta and L. Della Pietra. The squeeze film damper over four decades of investigations. part 2: Rotordynamic analyses with rigid and flexible rotors. *Shock and Vibration Digest*, 34(2):97–126, 2002.

[4] L. San Andrés. *Effect of Fluid Inertia on Squeeze Film Damper Force Response*. PhD thesis, Texas A&M University, 1985.

[5] L. San Andrés. Notes 13: Squeeze film dampers, 2010.

[6] L. San Andrés. Damping and inertia coefficients for two open ends squeeze film dampers with a central groove: Measurements and predictions. *Journal of Engineering for Gas Turbines and Power*, 134(10), 2012.

[7] L. San Andrés and S.-H. Jeung. Orbit-model force coefficients for fluid film bearings: A step beyond linearization. *Journal of Engineering for Gas Turbines and Power*, 138(2), 2015.

[8] L. San Andrés, S.-H. Jeung, S. Den, and G. Savela. Squeeze film dampers: An experimental appraisal of their dynamic performance. 2016.

[9] L. San Andrés and S. Seshagiri. Damping and inertia coefficients for two end sealed squeeze film dampers with a central groove: Measurements and predictions. *Journal of Engineering for Gas Turbines and Power*, 135(11), 2013.

[10] L. W. Barrett and E. J. Gunter. Steady-state and transient analysis of a squeeze film damper bearing for rotor stability. 1975.

[11] J. F. Booker. A table of the journal-bearing integral. *Journal of Basic Engineering*, 87(2):533–535, 1965.

[12] M. J. Braun and W. M. Hannon. Cavitation formation and modelling for fluid film bearings: A review. *Proceedings of the Institution of Mechanical Engineers, Part J: Journal of Engineering Tribology*, 224(9):839–863, 2010.

[13] G. Capone. Orbital motions of rigid symmetric rotor supported on journal bearings. *La Meccanica Italiana*, 199:37–46, 1986.

[14] D. Childs. *Turbomachinery Rotordynamics*. John Wiley & Sons, Inc., 1993.

[15] M. I. Friswell, J. E. T. Penny, S. D. Garvey, and A. W. Lees. *Dynamics of Rotating Machines*. Cambridge University Press, 2010.

[16] G. Genta. *Dynamics of Rotating Systems*. Springer, 2005.

[17] P. Hill and C. Peterson. *Mechanics and Thermodynamics of Propulsion*. Pearson Education, Inc., 1992.

[18] Y. Hori. *Hydrodynamic Lubrication*. Springer, 2006.

[19] Y. Ishida and T. Yamamoto. *Linear and Nonlinear Rotordynamics*. John Wiley & Sons, Inc., 2012.

[20] S. Y. Jung, L. San Andrés, and J. M. Vance. Measurements of pressure distributions and force coefficients in a squeeze film damper part 1: Fully open ended configuration. *Tribology Transactions*, 34(3):375–382, 1991.

[21] S. Y. Jung, L. San Andrés, and J. M. Vance. Measurements of pressure distributions and force coefficients in a squeeze film damper part 2: Partially sealed configuration. *Tribology Transactions*, 34(3):383–388, 1991.

[22] J. M. Krodkiewski and L. Sun. Modelling of multi-bearing rotor systems incorporating an active journal bearing. *Journal of Sound and Vibration*, 210(2):215–229, 1998.

[23] E. Krämer. *Dynamics of Rotors and Foundations*. Springer, 1993.

[24] M. C. Levesley and R. Holmes. The effect of oil supply and sealing arrangements on the performance of squeeze-film dampers: An experimental study. *Proceedings of the Institution of Mechanical Engineers, Part J: Journal of Engineering Tribology*, 210(4):221–232, 1996.

[25] J. W. Lund. Review of the concept of dynamic coefficients for fluid film journal bearings. *Journal of Tribology*, 109(1):37–41, 1987.

[26] J. D. Mattingly. *Elements of Propulsion: Gas Turbines and Rockets*. McGraw-Hill, 1996.

[27] L. Meirovitch. *Analytical Methods in Vibrations*. Macmillan, 1967.

[28] L. Meirovitch. *Elements of Vibration Analysis*. McGraw-Hill, 1975.

[29] C. Nataraj and H. D. Nelson. Periodic solutions in rotor dynamic systems with nonlinear supports: A general approach. *Journal of Vibration and Acoustics*, 111(2):187–193, 1989.

[30] H. D. Nelson and J. M. McVaugh. The dynamics of rotor-bearing systems using finite elements. *Journal of Engineering for Industry*, 98(2):593–600, 1976.

[31] O. Pinkus and B. Sternlicht. *Theory of Hydrodynamic Lubrication*. McGraw-Hill, 1961.

[32] Python. scipy.integrate.solve_ivp. `https://docs.scipy.org/doc/scipy/reference/generated/scipy.integrate.solve_ivp.html`.

[33] Python. scipy.optimize.fsolve. `https://docs.scipy.org/doc/scipy/reference/generated/scipy.optimize.fsolve.html`.

[34] E. Reinhardt and J. W. Lund. The influence of fluid inertia on the dynamic properties of journal bearings. *Journal of Lubrication Technology*, 97(2):159–165, 1975.

[35] M. H. Richardson and R. Potter. Viscous vs. structural damping in modal analysis. 1975.

[36] R. L. Ruhl and J. F. Booker. A finite element model for distributed parameter turborotor systems. *Journal of Engineering for Industry*, 94(1):126–132, 1972.

[37] J. T. Sawicki and T. V. V. L. N. Rao. Nonlinear prediction of rotordynamic coefficients for a hydrodynamic journal bearing. *Tribology Transactions*, 44(3):367–374, 2001.

[38] D. Scholz. Jet engines - bearings, seals and oil consumption, 2018.

[39] A. Z. Szeri. *Fluid Film Lubrication*. Cambridge University Press, 1980.

[40] J. M. Vance, F. Y. Zeidan, and B. G. Murphy. *Machinery Vibration and Rotordynamics*. John Wiley & Sons, Inc., 2010.

[41] F. Y. Zeidan, L. San Andrés, and J. M. Vance. Design and application of squeeze film dampers in rotating machinery. Texas A&M University. Turbomachinery Laboratories, 1996.